

# Dalton Transactions

An international journal of inorganic chemistry

Accepted Manuscript

This article can be cited before page numbers have been issued, to do this please use: P. Geysens, R. Heyns, R. Markowski, J. Ingenmey, L. Van Meervelt, A. Vlad, B. Kirchner, J. Fransaer and K. Binnemans, *Dalton Trans.*, 2026, DOI: 10.1039/D5DT02781K.



This is an Accepted Manuscript, which has been through the Royal Society of Chemistry peer review process and has been accepted for publication.

Accepted Manuscripts are published online shortly after acceptance, before technical editing, formatting and proof reading. Using this free service, authors can make their results available to the community, in citable form, before we publish the edited article. We will replace this Accepted Manuscript with the edited and formatted Advance Article as soon as it is available.

You can find more information about Accepted Manuscripts in the [Information for Authors](#).

Please note that technical editing may introduce minor changes to the text and/or graphics, which may alter content. The journal's standard [Terms & Conditions](#) and the [Ethical guidelines](#) still apply. In no event shall the Royal Society of Chemistry be held responsible for any errors or omissions in this Accepted Manuscript or any consequences arising from the use of any information it contains.

1

2 **Solvation structure of potassium bis(trifluoromethylsulfonyl)imide-glyme highly**

3 **concentrated electrolytes and cycling on organic cathodes**

4 Pieter Geysens,<sup>a</sup> Roy Heyns,<sup>a</sup> Robert Markowski,<sup>b</sup> Johannes Ingenmey,<sup>c</sup> Luc Van Meervelt,<sup>a</sup>  
5 Alexandru Vlad,<sup>b</sup> Barbara Kirchner,<sup>c</sup> Jan Fransaer<sup>d</sup> and Koen Binnemans<sup>†\*</sup>

6

7 <sup>a</sup>Department of Chemistry, KU Leuven, Celestijnenlaan 200F, P.O. box 2404, B-3001  
8 Leuven, Belgium.

9 <sup>b</sup>Institute of Condensed Matter and Nanosciences, UC Louvain, Place L. Pasteur 1, B-1348  
10 Louvain-la-Neuve, Belgium

11 <sup>c</sup>Mulliken Center for Theoretical Chemistry, University of Bonn, Bonn D-53115, Germany

12 <sup>d</sup>Department of Materials Engineering, KU Leuven, Kasteelpark Arenberg 44, B-3001  
13 Leuven, Belgium.

14

15

16

17 \*Corresponding author:

18 Email: [Koen.Binnemans@kuleuven.be](mailto:Koen.Binnemans@kuleuven.be)

19

1 **Abstract**View Article Online  
DOI: 10.1039/D5DT02781K

2 The physicochemical properties of highly concentrated electrolytes consisting of potassium  
3 bis(trifluoromethylsulfonyl)imide in oligo(ethyleneglycol) dimethyl ethers (glymes) are  
4 reported. The solvation structures were analyzed by Raman spectroscopy, single crystal X-ray  
5 diffraction, and theoretical calculations revealing significant ion-pairing at high  
6 concentrations especially for the shorter glymes, leading to them being classified as poor  
7 solvate ionic liquids with the general formula  $[K(L)_n][Tf_2N]$  ( $L = G1, G2, G3, \text{ or } G4; n = 2, 3$   
8 or 4).  $[K(G1)_2][Tf_2N]$  and  $[K(G2)_2][Tf_2N]$  had a sufficiently high ionic conductivity and were  
9 assessed as potential electrolytes in next-generation potassium-ion batteries. They were  
10 subjected to galvanostatic cycling on the new organic cathode material  $K_2\text{--Co--PTtSA}$ ,  
11 wherein PTtSA = benzene-1,2,4,5-tetra-methylsulfonamide. The results show a significantly  
12 improved capacity retention with these electrolytes, especially  $[K(G2)_2][Tf_2N]$  (91% after 200  
13 cycles), compared to a benchmark electrolyte consisting of 1 mol L<sup>-1</sup> KPF<sub>6</sub> in a mixture of  
14 ethylene carbonate and propylene carbonate (19% after 200 cycles). However, the  
15 performance at high C-rates was worse due to the high viscosities of highly concentrated  
16 electrolytes. This work shows that highly concentrated electrolytes and solvate ionic liquids  
17 can be promising electrolytes for next-generation potassium-ion batteries but can be further  
18 improved to reduce their viscosity and increase their ionic conductivity.

19

20 **Keywords:** alkali metals; electrolytes; glymes; non-aqueous coordination chemistry;  
21 potassium; solvates

22

## 1 Introduction

2 In the last decade, the focus on battery research has been shifted from lithium-ion batteries  
3 (LIBs) to sodium-ion batteries<sup>1</sup> (NIBs) and rechargeable magnesium metal batteries<sup>2</sup> (RMBs)  
4 due to the higher abundance and favorable properties of sodium and magnesium. More  
5 recently, potassium-ion batteries (KIBs) have also entered the scene of secondary battery  
6 research because of some desirable properties of the element potassium.<sup>3,4</sup> The reduction  
7 potential of the K<sup>+</sup>/K couple in organic electrolytes is even more negative than that of the  
8 Li<sup>+</sup>/Li couple, which opens the door to the design of high-voltage batteries (>4 V class) when  
9 combined with an appropriate cathode material.<sup>5,6</sup> Furthermore, because of its lower Lewis  
10 acidity, the K<sup>+</sup> cation interacts less strongly with its environment (solvents and electrode  
11 materials) compared to Li<sup>+</sup>, Na<sup>+</sup> and especially Mg<sup>2+</sup>, leading to higher ionic conductivities of  
12 the electrolytes and faster intercalation kinetics at the electrolyte-electrode interfaces.<sup>5,7,8</sup>  
13 Contrary to Na<sup>+</sup>, K<sup>+</sup> can also intercalate reversibly at reasonably high capacities  
14 (244 mAh g<sup>-1</sup>) into graphite anodes.<sup>5</sup> Potassium-containing electrolytes have been much less  
15 explored than new anode and cathode materials for reversible K<sup>+</sup> intercalation. Many  
16 potassium salts of interest for batteries such as KBF<sub>4</sub> and KClO<sub>4</sub> are barely soluble in the  
17 typical carbonate ester solvents such as ethylene carbonate (EC) and propylene carbonate  
18 (PC), due to their high lattice energy and the weak solvation of K<sup>+</sup> cations.<sup>6,8</sup> A “benchmark”  
19 electrolyte for KIBs is KPF<sub>6</sub> in a mixture of EC and PC, because of similarities with  
20 analogous Li<sup>+</sup> and Na<sup>+</sup> electrolytes and good passivation properties of the PF<sub>6</sub><sup>-</sup> anion with Al  
21 current collectors.<sup>9</sup> Unfortunately, batteries with this electrolyte typically suffer from large  
22 irreversible capacities in the initial cycles and low Coulombic efficiencies due to a poor solid  
23 electrolyte interface (SEI) formation on the anode.<sup>10-13</sup> Therefore, researchers are focusing  
24 more and more on the development of alternative electrolytes that do not have these issues of  
25 passivation and excessive chemical decomposition. One of the possible candidates are *highly*

1 *concentrated electrolytes* (HCEs), which have been extensively reported on in the context of [View Article Online](#)  
DOI: 10.1039/D5DT02781K

2 lithium-, sodium- and magnesium-based batteries.<sup>14-16</sup> HCEs are known to have several  
3 advantages compared to their dilute counterparts, such as increased oxidative and reductive  
4 stability, non-corrosive towards Al current collectors, decreased flammability and volatility,  
5 high charge carrier density, fast electrode reactions and decreased polysulfide solubility.<sup>17</sup>

6 Most importantly, because the salt anions are mostly coordinated to the cations in *contact ion*  
7 *pairs* (CIPs) or *aggregate* (AGG) solvate structures, they preferentially decompose over the  
8 solvent molecules, leading to an anion-derived robust inorganic SEI.<sup>18-22</sup> Studies on  
9 potassium-containing HCEs are still scarce. Xiao *et al.* were the first to report on the  
10 application of a HCE consisting of potassium bis(fluorosulfonyl)imide (KFSI) in 1,2-  
11 dimethoxyethane (DME, G1, monoglyme) with a molar ratio of 1:2, in an anode-less Cu|K  
12 battery.<sup>23</sup> They achieved stable cycling of dendrite-free potassium metal on the copper current  
13 collector with a Coulombic efficiency of 99%, indicating the formation of a stable and thin  
14 SEI. The overall electrochemical window of the HCE was 5 V, which allowed for coupling  
15 with a high-voltage Prussian Blue (KPB) cathode. Later, Hosaka *et al.* extended this work to  
16 the use of this HCE in a graphite|KFSI/DME|KPB full cell and achieved an impressive >85%  
17 capacity retention after 101 cycles with an average Coulombic efficiency of 99.3%.<sup>24</sup>

18 Replacing the DME solvent with longer glymes such as diethylene glycol dimethyl ether  
19 (diglyme, G2) or triethylene glycol dimethyl ether (triglyme, G3) was found to significantly  
20 enhance the oxidative stability of the HCEs, resulting in an increased cycling stability of full  
21 cells.<sup>25</sup> Xu *et al.* employed the strategy of adding a non-coordinating fluorinated diluent  
22 (1,1,2,2-tetrafluoro-1-(2,2,2-trifluoroethoxy)-ethane, TFETFE) to the KFSI/Glyme HCE in  
23 order to form a *localized high concentration electrolyte* (LHCE).<sup>26</sup> They achieved an  
24 unprecedented 83% capacity retention after 2000 cycles for K|KPB cells at a cut-off voltage  
25 of 4.3 V. Mandai *et al.* prepared several equimolar complexes of potassium salts with



1 pentaethylene glycol dimethyl ether (pentaglyme, G5) and reported phase diagrams, solvate  
2 structures and physicochemical properties.<sup>27</sup> Some of the complexes exhibited ionic-liquid-  
3 like behavior and could be classified as so-called *solvate ionic liquids* (SILs) or *liquid metal*  
4 *salts* (LMS). However, the authors did not report any electrochemical properties. Zeng *et al.*  
5 prepared a HCE (3.3 mol L<sup>-1</sup>) consisting of KFSI in trimethyl phosphate (TMP), which  
6 resulted in a non-flammable electrolyte for safe KIBs.<sup>28</sup> The authors achieved stable cycling  
7 of both graphite anodes and Prussian Blue cathodes with this HCE due to the formation of a  
8 stable and robust anion-derived SEI.

9 Here we report on the solvation structures such as *solvent separated ion pairs* (SSIPs),  
10 *contact ion pairs* (CIPs), and *aggregates* (AGGs) of several HCEs consisting of potassium  
11 bis(trifluoromethylsulfonyl)imide (KTf<sub>2</sub>N, KTFSI) dissolved in glymes (G1, G2, G3, G4),  
12 studied using Raman spectroscopy, single crystal X-ray diffraction (SCXRD), density  
13 functional theory (DFT) calculations, and molecular dynamics (MD) studies. Some of these  
14 HCEs can be classified as SILs and the dynamic viscosity, density, potassium concentration,  
15 and melting point or glass transition temperature of the complexes [K(L)<sub>n</sub>][Tf<sub>2</sub>N] (L = G1,  
16 G2, G3, or G4; n = 2, or 3) are also reported. As a proof of concept, we demonstrate the  
17 charge-discharge cycling results of [K(G1)<sub>2</sub>][Tf<sub>2</sub>N] and [K(G2)<sub>2</sub>][Tf<sub>2</sub>N], with the organic  
18 cathode material K<sub>2</sub>–Co–PTtSA, wherein PTtSA = benzene-1,2,4,5-tetra-methylsulfonamide,  
19 in a coin-cell configuration.



## 1 Experimental

## 2 Materials and synthesis

3 Potassium bis(trifluoromethylsulfonyl)imide (KTf<sub>2</sub>N, KTFSI, 99.5%) was purchased from  
4 Solvionic (Toulouse, France) and was dried at 120 °C for 24 h on a vacuum line prior to use.  
5 1,2-Dimethoxyethane (monoglyme, G1, 99+, extra dry over molecular sieves) and 1-  
6 methoxy-2-(2-methoxyethoxy)ethane (diglyme, G2, 99+, extra dry over molecular sieves)  
7 were purchased from Fisher Scientific (Brussels, Belgium) and were used as received. 1,2-  
8 Bis(2-methoxyethoxy)ethane (triglyme, G3, 99%) and bis[2-(2-methoxyethoxy)ethyl] ether  
9 (tetraglyme, G4, 99%) were purchased from Fisher Scientific (Brussels, Belgium) and dried  
10 prior to use over freshly activated molecular sieves (3 Å, 1 to 2 mm) which were purchased  
11 from Alfa Aesar (Belgium). The water content of the glymes was measured by a Mettler-  
12 Toledo C30S coulometric Karl Fischer titrator and was found to be lower than 50 ppm, in  
13 accordance of the specification provided by the manufacturer. Ferrocenium  
14 hexafluorophosphate (FcPF<sub>6</sub>, 97%) was purchased from Merck (Darmstadt, Germany) and  
15 was used as received. Ferrocene (Fc, purum, ≥ 98%) was purchased from Fluka (Bucharest,  
16 Romania) and was used as received. *N*-butyl-*N*-methylpyrrolidinium  
17 bis(trifluoromethylsulfonyl)imide ([BMP][Tf<sub>2</sub>N], 99%) was purchased from IoLiTec  
18 (Heilbronn, Germany) and was dried at 110 °C for 48 h on a vacuum line prior to use. Storage  
19 of the reagents and all the manipulations involving contact of the chemicals with the  
20 atmosphere were performed in an argon-filled glovebox with an oxygen and water  
21 concentration below 1 ppm. The solvate ionic liquids were prepared by adding a  
22 stoichiometric amount of glyme to KTf<sub>2</sub>N in glass vials, which were closed with airtight  
23 screwcaps afterwards, and subsequently heating the mixture under stirring until a  
24 homogeneous liquid was obtained. The liquids were then allowed to cool down to ambient  
25 glovebox temperature (~28 °C).

## 1 Methods

2 Melting points were determined on a Mettler-Toledo DSC-1 instrument at a heating rate of  
3  $10\text{ }^{\circ}\text{C min}^{-1}$  under a helium atmosphere. Aluminium crucibles were filled with samples of  
4 electrolyte (3 to 12 mg) inside an argon-filled glovebox and sealed to prevent contact with the  
5 air. The samples were cycled twice (heating first) between  $-80\text{ }^{\circ}\text{C}$  and  $100\text{ }^{\circ}\text{C}$ . The melting  
6 point values determined in the second cycle are reported. Thermogravimetric analysis (TGA)  
7 was performed on a TA Instruments TGA Q500 at a heating rate of  $5\text{ }^{\circ}\text{C min}^{-1}$  under a  
8 nitrogen atmosphere with a flow rate of  $60\text{ mL min}^{-1}$ . The sample size was typically between  
9 5 and 10 mg. In order to make the TGA traces of the different samples directly comparable,  
10 the data (mass vs. time) was normalized by dividing by their initial mass value. The data on  
11 the y-axis is expressed as the remaining fraction of the initial sample mass (in %). The  
12 viscosity and density of the electrolytes were measured on a Lovis 2000 ME rolling-ball  
13 microviscometer and a DMA 4500 M density meter, respectively. To avoid contact with air,  
14 the samples were transferred from their sealed argon-filled containers to a syringe and  
15 subsequently injected into the capillaries or density chamber of the device. The temperature  
16 during both the viscosity and density measurements was controlled by the internal thermostat  
17 of the device. The specific ionic conductivity of the electrolytes was measured using a  
18 Mettler-Toledo SevenCompact Cond S230 conductivity meter equipped with an InLab 751-  
19 4mm glass probe with two platinum poles. The instrument was calibrated using aqueous  
20 standards with a known specific ionic conductivity. The probe was submerged in the  
21 electrolytes at ambient temperature (approximately  $25\text{ }^{\circ}\text{C}$ ) and the setup was allowed to  
22 stabilize. Contact of the samples with ambient air was unavoidable during the measurement.  
23 FT-Raman spectra were recorded between  $3500\text{ cm}^{-1}$  and  $50\text{ cm}^{-1}$  on a Bruker Vertex 70  
24 spectrometer with a RamII Raman module and a liquid-nitrogen-cooled germanium diode  
25 detector. Each measurement consisted of 64 scans at a resolution of  $2\text{ cm}^{-1}$  with a 1064.38 nm

1 laser (Nd:YAG) at a power of 500 mW. Samples were measured inside 2 mL glass vials that  
2 were filled inside the glovebox and subsequently closed with airtight screwcaps. Single  
3 crystal X-ray diffraction measurements were performed on  $[K(G3)_2][Tf_2N]$ . Single crystals  
4 were obtained by slow cooling of a concentrated solution of the complex in G3. A suitable  
5 crystal was selected and placed on a Bruker D8 Venture diffractometer. The crystal was kept  
6 at 100(2) K during data collection. Using Olex2,<sup>29</sup> the structure was solved with the  
7 SHELXT<sup>30</sup> structure solution program using Intrinsic Phasing and refined with the  
8 SHELXL<sup>31</sup> refinement package using Least Squares minimization. All H atoms were placed  
9 in calculated positions and treated as riding on their parent atoms, with C-H = 0.93-0.98 Å,  
10  $U_{iso}(H) = 1.2$  or  $1.5 U_{eq}(C)$ . The asymmetric unit consists of two half  $Tf_2N^-$  anions (the two  
11 remaining halves are generated by inversion centers) and are disordered over several  
12 positions. The first half was refined with two positions, but the second half was too disordered  
13 to refine. Therefore, the solvent mask procedure was used during the refinement. A cavity of  
14 311 Å<sup>3</sup> with therein 140 electrons ( $Tf_2N^-$  = 138 electrons) was used. All the electrochemical  
15 measurements were performed inside an argon-filled glovebox with water and oxygen  
16 concentrations below 1 ppm. Cyclic voltammograms (CVs) were measured using an Autolab  
17 PGSTAT302N potentiostat and Nova 2.1 software. The working electrodes for CV were  
18 pieces of silicon wafer, coated with 500 nm of silica, 10 nm of titanium and 100 nm of  
19 platinum (Imec, Belgium) (surface area of 0.3 cm<sup>2</sup>), the counter electrode a larger piece of  
20 platinum-coated silicon wafer (surface area of approx. 1.0 cm<sup>2</sup>) and the scan rate was  
21 10 mV s<sup>-1</sup>. The reference electrode consisted of a platinum wire, submerged in a solution of  
22 ferrocene (Fc) and ferrocenium hexafluorophosphate ( $FcPF_6$ ) (5 mmol L<sup>-1</sup> each) in the ionic  
23 liquid *N*-butyl-*N*-methylpyrrolidinium bis(trifluoromethylsulfonyl)imide ( $[BMP][Tf_2N]$ ),  
24 contained inside a fritted glass tube (referred to as  $Fc^+/Fc$ ). The CVs were started at open  
25 circuit potential (OCP) and are uncorrected for Ohmic drop. The galvanostatic cycling tests



1 were carried out using 2025-type coin cells with a 13 mm diameter active carbon fabric as the  
2 counter/reference electrodes and glass microfiber filters as the separators. The positive  
3 electrode composition was made by hand-grinding 50 wt.% active material ( $K_2$ –Co–benzene–  
4 1,2,4,5-tetra-methylsulfonamide) with 40 to 10 wt.% conductive carbon (Super P) and 10  
5 wt.% PTFE as a binder.<sup>32</sup> The electrodes were manufactured by applying the composite  
6 powder to the positive side of the coin cell case (CR 2032, AISI 316L stainless steel) and  
7 compacting with a stainless-steel disk. The active material loading is approximately 1.5–2  
8 mg, with a surface density of approximately  $3 \text{ mg cm}^{-2}$  (corresponding to approx.  $6 \text{ mg cm}^{-2}$   
9 of composite), with an electrode thickness of approx. 0.15 mm. The electrode porosity was  
10 not quantitatively evaluated. However, SEM observations indicate that the electrode is  
11 slightly compressed while retaining sufficient porosity, enabling effective electrolyte  
12 penetration throughout the composite electrode. At room temperature, galvanostatic  
13 charge/discharge experiments were conducted using a Neware battery testing equipment. As  
14 electrolyte,  $1 \text{ mol L}^{-1}$   $KPF_6$  in EC:PC,  $[K(G1)_2][Tf_2N]$  and  $[K(G2)_2][Tf_2N]$  were used. A  
15 GF/D glass-fiber separator was used, and  $150 \mu\text{L}$  of electrolyte was added to each cell. The  
16 long-term stability tests were performed at a cycling rate of C/10.

## 17 Theoretical calculations

18 Classical molecular dynamics (MD) simulations were performed using the LAMMPS  
19 program package (version of 23 June 2022).<sup>33</sup> The composition and final box dimensions of  
20 the simulated systems are given in the Supporting Information (Table S6). OPLS-AA<sup>34</sup> force  
21 field parameters were employed for the glymes, the  $Tf_2N^-$  anion, and the  $K^+$  cation.<sup>35</sup>  
22 Geometric mixing rules were applied for non-bonded interactions between unlike atoms.<sup>36</sup>  
23 The cutoff for Lennard-Jones and Coulombic interactions was set to 1.2 nm. Initial  
24 configurations were created randomly using the PACKMOL tool.<sup>37</sup> Bulk simulations of  $Gn$ –  
25  $KTf_2N$  with  $n = 1$ –4 at compositions of 1:2, 1:3, and 1:4 were carried out in cubic boxes,



1 employing periodic boundary conditions in all directions. The systems were equilibrated over  
2 a total simulation time of 35 ns in the NVE, NpT, and NVT ensemble. After an initial energy  
3 minimization, the system was simulated for 250 ps in the NVE ensemble with added velocity  
4 scaling corresponding to a temperature of 500 K. Afterwards, the systems were simulated for  
5 14 ns in the NpT ensemble. The Nosé-Hoover chain thermostat and barostat were applied to  
6 achieve a constant pressure of 1.01325 bar and a temperature of 350.15 K.<sup>38,39</sup> The average  
7 volume of the latter 10 ns was then used as final box volume for the subsequent equilibration  
8 of 21 ns in the NVT ensemble. Finally, a production run of 10 ns was carried out in the NVT  
9 ensemble. The timestep was set to 1.0 fs and every 1000th step was saved in a trajectory for  
10 further processing.

11 Quantum chemical calculations were carried out at the DFT level of theory using the ORCA  
12 5.0 program package.<sup>40</sup> The B3LYP functional was employed in combination with the def2-  
13 TZVP basis set. The D3 dispersion correction<sup>41,42</sup> was applied to account for London  
14 dispersion interactions. Grimme's geometrical counterpoise<sup>43</sup> correction was used to deal with  
15 the inter-molecular as well as intra-molecular basis set superposition error. Tight SCF  
16 convergence criteria were applied for all calculations. Harmonic frequencies were calculated  
17 as analytical derivatives of the energy gradient to ensure the absence of imaginary modes.  
18 Electrochemical reduction and oxidation potentials were calculated following the adiabatic  
19 thermodynamic cycle method:<sup>44,45</sup>

$$20 \quad U_{red}(R) = \frac{E(R) - E(R^-)}{nF} - U_{ref}$$

$$21 \quad U_{ox}(R) = \frac{E(R^+) - E(R)}{nF} - U_{ref}$$

22 where  $E(R)$ ,  $E(R^-)$ , and  $E(R^+)$  are the electronic energy of compound or complex R in its  
23 neutral, reduced, and oxidized form, respectively, and  $U_{ref} = 1.549$  V to account for the

1 difference between the absolute potential scale and K/K<sup>+</sup>. The conductor-like polarizable [View Article Online](#)  
2 continuum model (CPCM) was employed to implicitly account for solvation effects.<sup>46</sup> The  
3 relative permittivity was set to each glyme's respective experimental value ( $\epsilon_r(G1) = 7.1$ ,  
4  $\epsilon_r(G2) = 7.4$ ,  $\epsilon_r(G3) = 7.6$ , and  $\epsilon_r(G4) = 7.8$ ), while all other CPCM parameters were kept at  
5 their default values.<sup>47</sup>

6

## 7 **Synthesis and characterization data of complexes**

8 [K(G1)<sub>2</sub>][Tf<sub>2</sub>N]

9 A mixture of KTf<sub>2</sub>N (1.000 g, 3.132 mmol) and G1 (0.565 g, 6.265 mmol) was stirred inside a  
10 closed glass vial at 60 °C under argon until complete dissolution of the solid. Upon cooling,  
11 the mixture remained a homogeneous liquid and [K(G1)<sub>2</sub>][Tf<sub>2</sub>N] (1.565 g, 3.132 mmol, 100%  
12 yield) was isolated as a clear colorless viscous liquid. (FT-Raman shifts/cm<sup>-1</sup>): 2999, 2954,  
13 2930, 2903, 2832, 1476, 1455, 1246, 1140, 860, 744, 407, 366, 353, 339, 327, 314, 298, 280,  
14 119. Glass transition point: -56 °C.

15 [K(G1)<sub>3</sub>][Tf<sub>2</sub>N]

16 A mixture of KTf<sub>2</sub>N (1.001 g, 3.136 mmol) and G1 (850 g, 9.432 mmol) was stirred inside a  
17 closed glass vial at 60 °C under argon until complete dissolution of the solid. Upon cooling,  
18 the mixture remained a homogeneous liquid and [K(G1)<sub>3</sub>][Tf<sub>2</sub>N] (1.851g, 3.139 mmol, 100%  
19 yield) was isolated as a clear colorless viscous liquid. (FT-Raman shifts/cm<sup>-1</sup>): 2996, 2952,  
20 2930, 2901, 2831, 1476, 1454, 1287, 1245, 1140, 860, 743, 406, 365, 339, 326, 313, 298, 280,  
21 119. Melting point: -33 °C.

22 [K(G1)<sub>4</sub>][Tf<sub>2</sub>N]

1 A mixture of  $\text{KTf}_2\text{N}$  (0.999 g, 3.129 mmol) and G1 (1.130 g, 12.539 mmol) was stirred inside  
2 a closed glass vial at 60 °C under argon until complete dissolution of the solid. Upon cooling,  
3 the mixture remained a homogeneous liquid and  $[\text{K}(\text{G1})_4][\text{Tf}_2\text{N}]$  (2.129 g, 3.132 mmol, 100%  
4 yield) was isolated as a clear colorless viscous liquid. (FT-Raman shifts/cm<sup>-1</sup>): 2993, 2950,  
5 2928, 2900, 2830, 2726, 1476, 1453, 1245, 1140, 860, 743, 406, 366, 339, 326, 313, 297, 280,  
6 119. Melting point: not observed.

7  $[\text{K}(\text{G2})_2][\text{Tf}_2\text{N}]$

8 A mixture of  $\text{KTf}_2\text{N}$  (1.002 g, 3.139 mmol) and G2 (841 g, 6.265 mmol) was stirred inside a  
9 closed glass vial at 60 °C under argon until complete dissolution of the solid. Upon cooling,  
10 the mixture remained a homogeneous liquid and  $[\text{K}(\text{G2})_2][\text{Tf}_2\text{N}]$  (1.843 g, 3.137 mmol, 100%  
11 yield) was isolated as a clear colorless viscous liquid. (FT-Raman shifts/cm<sup>-1</sup>): 2950, 2901,  
12 2835, 2751, 1476, 1450, 1336, 1282, 1245, 1139, 868, 840, 743, 573, 406, 326, 313, 298, 279,  
13 119. Melting point: -8 °C.

14  $[\text{K}(\text{G2})_3][\text{Tf}_2\text{N}]$

15 A mixture of  $\text{KTf}_2\text{N}$  (0.998 g, 3.126 mmol) and G2 (1.258 g, 9.376 mmol) was stirred inside a  
16 closed glass vial at 60 °C under argon until complete dissolution of the solid. Upon cooling,  
17 the mixture remained a homogeneous liquid and  $[\text{K}(\text{G2})_3][\text{Tf}_2\text{N}]$  (2.256 g, 3.126 mmol, 100%  
18 yield) was isolated as a clear colorless viscous liquid. (FT-Raman shifts/cm<sup>-1</sup>): 2949, 2895,  
19 2833, 2751, 1476, 1452, 1282, 1244, 1139, 868, 840, 742, 572, 405, 326, 313, 298, 279, 167,  
20 119. Melting point: -4 °C.

21  $[\text{K}(\text{G3})_2][\text{Tf}_2\text{N}]$

22 A mixture of  $\text{KTf}_2\text{N}$  (1.001 g, 3.136 mmol) and G3 (1.120 g, 6.284 mmol) was stirred inside a  
23 closed glass vial at 60 °C under argon until complete dissolution of the solid. Upon cooling,  
24 the mixture crystallized and  $[\text{K}(\text{G3})_2][\text{Tf}_2\text{N}]$  (2.121 g, 3.139 mmol, 100% yield) was isolated

1 as a clear colorless crystalline solid. (FT-Raman shifts/cm<sup>-1</sup>): 2944, 2925, 2899, 2852, 2826  
2 1478, 1448, 1273, 1244, 1144, 1134, 872, 840, 741, 341, 314, 305, 281, 123, 102. Melting  
3 point: 45 °C.

4 [K(G4)][Tf<sub>2</sub>N]

5 A mixture of KTF<sub>2</sub>N (1.000 g, 3.132 mmol) and G4 (0.696 g, 3.132 mmol) was stirred inside a  
6 closed glass vial at 60 °C under argon until complete dissolution of the solid. Upon cooling,  
7 the mixture crystallized and [K(G4)][Tf<sub>2</sub>N] (1.696 g, 3.132 mmol, 100% yield) was isolated  
8 as a clear colorless crystalline solid. (FT-Raman shifts/cm<sup>-1</sup>): 2952, 2903, 2864, 2841, 1477,  
9 1456, 1280, 1244, 1141, 866, 835, 742, 558, 398, 341, 326, 314, 298, 279, 121. Melting point:  
10 36 °C.

11 [K(G4)<sub>2</sub>][Tf<sub>2</sub>N]

12 A mixture of KTF<sub>2</sub>N (0.999 g, 3.129 mmol) and G4 (1.392 g, 6.262 mmol) was stirred inside a  
13 closed glass vial at 60 °C under argon until complete dissolution of the solid. Upon cooling,  
14 the mixture remained a homogeneous liquid and [K(G4)<sub>2</sub>][Tf<sub>2</sub>N] (2.391 g, 3.130 mmol, 100%  
15 yield) was isolated as a clear colorless viscous liquid. (FT-Raman shifts/cm<sup>-1</sup>): 2891, 2834,  
16 1476, 1452, 1337, 1281, 1243, 1139, 866, 836, 741, 572, 405, 339, 326, 312, 297, 279, 165,  
17 120. Melting point: 19 °C.

18

19

20



## 1 Results and discussion

### 2 *Physicochemical properties of glyme-KTf<sub>2</sub>N binary mixtures*

3 When KTf<sub>2</sub>N is dissolved in glymes, the K<sup>+</sup> cations are solvated by the ether oxygen atoms of  
4 the glyme molecules, leading to the formation of solvate complexes. Several possible solvate  
5 complex structures are defined, depending on the number of anions in the primary  
6 coordination shell around the K<sup>+</sup> cations (Figure 1). *Solvent separated ion pairs* (SSIPs) are  
7 structures where the K<sup>+</sup> cations are completely separated from the anions by a primary  
8 coordination shell consisting of only solvent molecules. *Contact ion pairs* (CIPs) are neutral  
9 complexes where the K<sup>+</sup> cations are solvated by solvent molecules as well as one anion.  
10 Depending on the coordination of the anion, CIP I and CIP II can be distinguished, where the  
11 anion coordinates in a monodentate or bidentate manner, respectively. In *aggregates* (AGGs),  
12 several K<sup>+</sup> cations are linked together by two (AGG I) or three (AGG II) anions, resulting in  
13 large polymeric coordination networks. In any solution of KTf<sub>2</sub>N in glymes, these different  
14 solvation structures exist in equilibrium with each other due to the kinetically labile nature of  
15 alkali metal ion complexes.

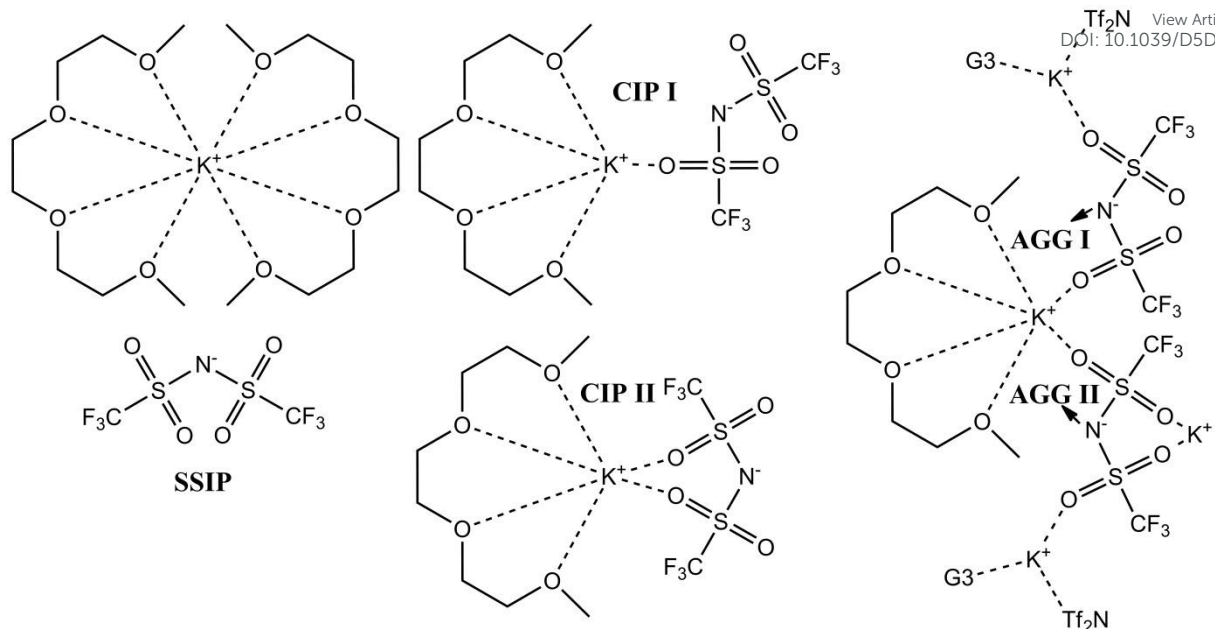
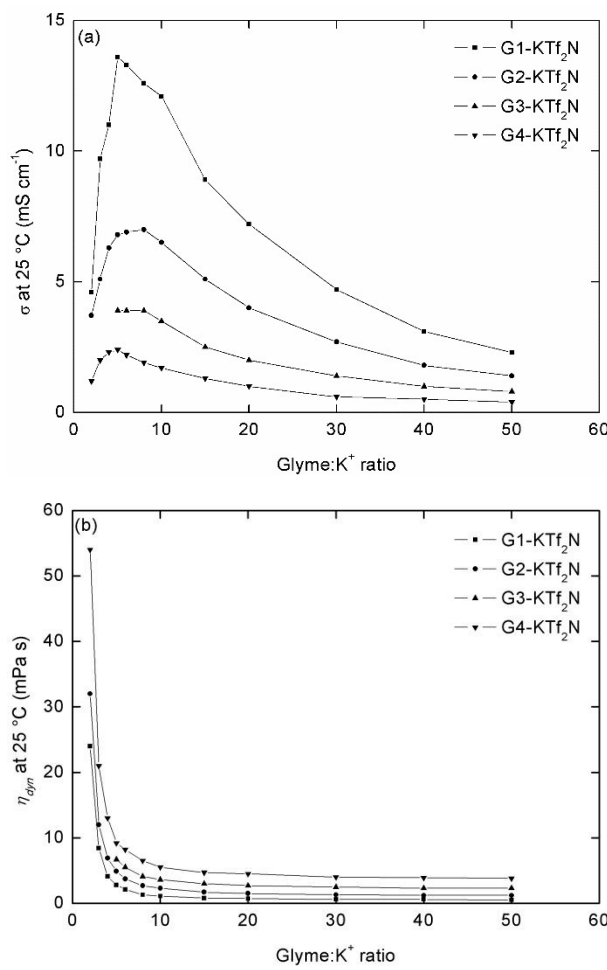


**Figure 1.** Schematic representation of the three main solvated species in  $\text{KTf}_2\text{N}$ –triglyme binary mixtures: solvent separated ion pairs (SSIP) (left), contact ion pairs (CIP I and CIP II) (middle), and aggregate structures (AGG I and AGG II) (right).

1  
 2 Mixtures of the glymes monoglyme (G1), diglyme (G2), triglyme (G3), and tetraglyme (G4)  
 3 with potassium bis(trifluoromethylsulfonyl)imide ( $\text{KTf}_2\text{N}$ ) with glyme: $\text{KTf}_2\text{N}$  ratios ranging  
 4 from 50:1 to 1:1 were prepared. It was found that even at high concentrations of  $\text{KTf}_2\text{N}$ ,  
 5 homogeneous liquid mixtures were obtained, indicating a high solubility of this salt in the  
 6 glyme solvents. This can be explained by the excellent electron-withdrawing properties of the  
 7  $-\text{SO}_2\text{CF}_3$  groups in the anion resulting in efficient electron delocalization. For the G1 and G2  
 8 series of mixtures, only at a 1:1 ratio, inhomogeneous (liquid + solid) mixtures were  
 9 observed, indicating a solubility limit. For the G3 series of mixtures, crystals were observed at  
 10 a 4:1 ratio and below and the 2:1 ratio mixture was a homogeneous solid. These crystals were  
 11 analyzed by single crystal X-ray diffraction and it was revealed that the crystalline solid was  
 12 the solvate complex  $[\text{K}(\text{G3})_2][\text{Tf}_2\text{N}]$  (*vide infra*). For the G4: $\text{KTf}_2\text{N}$  series, every mixture was  
 13 a homogeneous liquid except the 1:1 mixture, which was a homogeneous crystalline solid. In

1 order to assess the suitability of these glyme– $\text{KTf}_2\text{N}$  mixtures as electrolytes in batteries, their  
 2 physicochemical properties such as specific ionic conductivity ( $\sigma$ ), dynamic viscosity ( $\eta_{dyn}$ ),  
 3 density ( $\rho$ ) and potassium-ion concentration were determined. The numerical values are  
 4 summarized in the ESI (Tables S1–S4). A plot of the specific ionic conductivity and the  
 5 dynamic viscosity *vs.* the glyme: $\text{KTf}_2\text{N}$  ratio is shown in Figure 2.



7 **Figure 2.** Specific ionic conductivity (a) and dynamic viscosity (b) of electrolytes *vs.* the  
 8 glyme: $\text{KTf}_2\text{N}$  ratio, measured at 25 °C. Some datapoints are missing for the G3– $\text{KTf}_2\text{N}$  series  
 9 because of the presence of crystals in the solution.



1

2 The specific ionic conductivity is a very important parameter to describe an electrolyte, since  
3 it has a significant influence on the current densities that can be achieved during  
4 charge–discharge cycling experiments, and therefore the C-rate performance (*vide infra*). The  
5 specific ionic conductivity is determined by two factors: (1) the total concentration of charge  
6 carriers (ions) and (2) the mobility of those charge carriers. The mobility, in turn, depends on  
7 the dynamic viscosity of the electrolyte and the nature of the solvate species that are present  
8 in solution. Neutral species such as contact ion pairs (CIPs) are not attracted to the electrodes  
9 as opposed to charged species such as solvent separated ion pairs and are therefore less  
10 mobile. The solvation in these glyme– $\text{KTf}_2\text{N}$  electrolytes is extensively discussed below. In  
11 Figure 2a, a typical maximum curve can be observed for the conductivity in function of the  
12 glyme: $\text{KTf}_2\text{N}$  ratio. This can be explained by the two competing factors: the ion concentration  
13 and the ion mobility (*i.e.* the viscosity). In relatively dilute conditions, the total ion  
14 concentration is dominant over the small increase in viscosity, as the fraction of salt in the  
15 electrolytes is increased. This results in the initial increase in conductivity. However, as the  
16 salt fraction (ion concentration) is further increased, the viscosity is increasing more strongly  
17 (Figure 2b), and it becomes the dominant factor, resulting in a decrease of the conductivity.  
18 The maximum conductivity is usually reached at the 5:1 glyme: $\text{KTf}_2\text{N}$  composition, except  
19 for the G2 series of electrolytes, where it is observed at the 8:1 composition. However, the  
20 change in conductivity compared to the 5:1 is rather small and within the margin of error of  
21 the conductometer. It should be noted that some data points are missing for the G3 series of  
22 electrolytes because crystals started forming at ratios of 4:1 and below, but it is likely that the  
23 conductivity would also have decreased for these compositions in this case. When the  
24 different glyme series are compared, it is evident that the conductivity decreases with  
25 increasing glyme length. This is because for the same glyme: $\text{KTf}_2\text{N}$  ratio, the  $\text{K}^+$

View Article Online  
DOI: 10.1039/D5DT02781K

1 concentration is actually lower for the longer glymes due to their increased molar volume  
2 Furthermore, the viscosity of the glymes also increases with increasing chain length (G1: 0.5  
3 mPa s, G2: 1.0 mPa s, G3: 2.0 mPa s, and G4: 3.4 mPa s at 25 °C) due to the stronger dipole  
4 and Van der Waals interactions. Interestingly, the decrease in conductivity with the  
5 glyme:KTf<sub>2</sub>N ratio is very sharp for the G1 series of electrolytes as opposed to the longer  
6 glyme series where it is much more gradual. This can possibly be explained by differences in  
7 the solvation structures that are present in solution, *i.e.* a higher degree of CIP and AGG  
8 formation in the G1 electrolytes. Overall, the specific ionic conductivities of the  
9 glyme–KTf<sub>2</sub>N electrolytes, especially the G1 and G2 series, are in an acceptable range, even  
10 for the highly concentrated examples.

11 At well-defined stoichiometric ratios of salt and glyme, it might be possible to isolate the  
12 solvate complexes in the solid (crystalline) state. Therefore, the most concentrated  
13 glyme–KTf<sub>2</sub>N mixtures were analyzed by differential scanning calorimetry (DSC) in order to  
14 determine the melting points (T<sub>m</sub>) of these solvate complexes of the general form  
15 [K(Gn)<sub>x</sub>][Tf<sub>2</sub>N] (n = 1–4). The expected coordination number of K<sup>+</sup> in glymes is between 8  
16 and 10, according to Mandai *et al.*, so this would correspond to 4 G1, 3 G2, 2 G3 and 2 G4  
17 ligands, if only K<sup>+</sup>–solvent interactions are considered.<sup>48</sup> Mixtures with a higher  
18 glyme:KTf<sub>2</sub>N ratio were not measured. These solvate complexes are technically considered  
19 highly concentrated electrolytes (HCEs) consisting of KTf<sub>2</sub>N dissolved in glymes. However,  
20 if certain criteria are met, these HCEs can also start exhibiting typical behavior associated  
21 with ionic liquids, so-called *solvate ionic liquids* (SILs). Mandai *et al.* have proposed five  
22 criteria to distinguish SILs from typical HCEs:<sup>49</sup> (1) they must be solvate compounds between  
23 an ion and a ligand(s) in a certain stoichiometric ratio; (2) they must consist entirely of  
24 complex ions (solvates) and their counterions in the molten state; (3) they must show no  
25 physicochemical properties based on both pure ligands and precursor salts under using

1 conditions; (4) they must have a melting point below 100 °C to satisfy the criterion for typical  
 2 ILs; and (5) they must have a negligible vapor pressure under typical application conditions.  
 3 In many cases, these criteria are only partially met. In that instance, the HCEs are classified as  
 4 “poor” SILs. Table 1 summarizes the melting points of the different solvate complexes. For  
 5 some mixtures, a well-defined melting point was not observed and the glass transition  
 6 temperature ( $T_g$ ) is shown in those cases.

7

**Table 1.** Melting Points ( $T_m$ ) and GlassTransition ( $T_g$ ) Temperatures

Complex	$T_m^a$ (°C)	$T_g^a$ (°C)
[K(G1) <sub>4</sub> ][Tf <sub>2</sub> N]	n.o.	n.o.
[K(G1) <sub>3</sub> ][Tf <sub>2</sub> N]	-33	n.o.
[K(G1) <sub>2</sub> ][Tf <sub>2</sub> N]	n.o.	-58
[K(G2) <sub>3</sub> ][Tf <sub>2</sub> N]	-4	n.o.
[K(G2) <sub>2</sub> ][Tf <sub>2</sub> N]	-8	n.o.
[K(G3) <sub>2</sub> ][Tf <sub>2</sub> N]	45	n.o.
[K(G4) <sub>2</sub> ][Tf <sub>2</sub> N]	19	n.o.
[K(G4)][Tf <sub>2</sub> N]	36	n.o.

<sup>a</sup>n.o.: not observed

8

9 In general, the observed melting points of the solvate complexes are well below 100 °C, with  
 10 most of them even below room temperature (25 °C), thereby satisfying criterion 4. This is  
 11 typical for complexes with the highly delocalized and flexible  
 12 bis(trifluoromethylsulfonyl)imide anion that inhibits crystallization. As the glyme chain  
 13 length increases, the melting point of the corresponding solvate complexes clearly increases



1 as well. For the complexes with G1 ligands, the melting point is either below -30 °C or not.  
View Article Online  
DOI: 10.1039/D5DT02781K

2 observed at all. For the complexes with G2 ligands, the melting point is just below 0 °C, and  
3 for the G3 and G4 complexes, the melting point is around or just above room temperature  
4 (25 °C).

5 In order to evaluate criterion 5, the thermal stability of the solvate complexes was investigated  
6 by dynamic thermogravimetric analysis (TGA) and compared to the pure glymes and pure  
7  $\text{KTf}_2\text{N}$  (ESI Figure S1–S4). The pure  $\text{KTf}_2\text{N}$  salt does not form any hydrates and is thermally  
8 stable to a temperature of approx. 400 °C, at which point the anion starts to decompose. Upon  
9 comparing the TGA traces of the solvate complexes with those of the pure glymes (ligands),  
10 an enhanced thermal stability is clearly observed for the complexes over the ligands.

11 However, the overall thermal stability of the G1 and G2 solvate complexes is still quite poor,  
12 as most of the glymes are evaporated at a temperature of approx. 100 °C. The complex  
13  $[\text{K}(\text{G}3)_2][\text{Tf}_2\text{N}]$  is slightly more stable, and  $[\text{K}(\text{G}4)_2][\text{Tf}_2\text{N}]$  and  $[\text{K}(\text{G}4)][\text{Tf}_2\text{N}]$  even more so,  
14 where the latter one is even thermally stable beyond 100 °C. This trend is of course expected  
15 according to the chelate effect of the glyme ligands, as well as their respective boiling points  
16 (85, 162, 216 and 275 °C for G1, G2, G3 and G4 respectively). Interestingly, the mass of  
17  $[\text{K}(\text{G}1)_4][\text{Tf}_2\text{N}]$  and  $[\text{K}(\text{G}1)_3][\text{Tf}_2\text{N}]$  does not decrease to the theoretical value after loss of all  
18 ligands. However this can be explained by premature evaporation of the highly volatile G1  
19 ligand before the actual TGA measurement starts. For all the other complexes with longer  
20 glyme ligands, the theoretical remaining mass values are reached.  $[\text{K}(\text{G}4)][\text{Tf}_2\text{N}]$  also starts  
21 losing ligands at a higher temperature than  $[\text{K}(\text{G}4)_2][\text{Tf}_2\text{N}]$ , so it appears that the second G4  
22 ligand is more weakly coordinated to  $\text{K}^+$  than the first one. This is also expected, taking into  
23 account the significant steric hindrance associated with the coordination of two complete G4  
24 ligands.

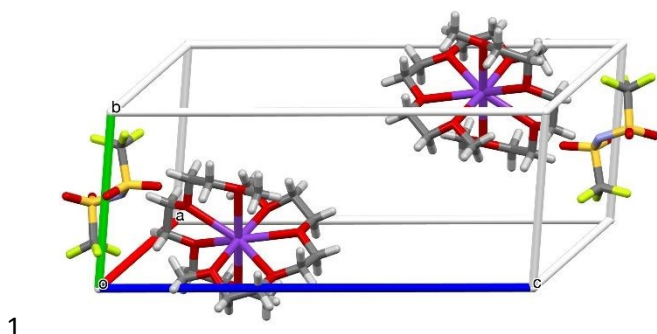
25

1 *Solvation study of glyme-KTf<sub>2</sub>N binary mixtures*

2 Criteria 1 and 2, which were proposed by Mandai *et al.*, both relate to the solvate structure of  
3 the isolated complexes in the solid as well as the liquid state.<sup>49</sup> In general, it is advantageous  
4 to study these solvate structures because they provide useful insights into the performance of  
5 the batteries that are constructed with these HCEs/SILs. The solvation structure of solids can  
6 be revealed by single crystal X-ray diffraction (XRD) techniques as well as Raman  
7 spectroscopy and those of liquids by Raman spectroscopy as well. Theoretical calculations  
8 such as density functional theory (DFT) and molecular dynamics (MD) can also aid to  
9 interpret the experimentally observed data.

10 Of the eight solvate complexes that were prepared, only two were crystalline solids at room  
11 temperature: [K(G3)<sub>2</sub>][Tf<sub>2</sub>N] and [K(G4)][Tf<sub>2</sub>N]. Of these two, [K(G4)][Tf<sub>2</sub>N] had the  
12 tendency to form a undercooled liquid upon cooling the melt and form a polycrystalline mass  
13 upon crystallizing, so no single crystals of a sufficiently high quality for single crystal XRD  
14 were obtained. Good-quality single crystals of [K(G3)<sub>2</sub>][Tf<sub>2</sub>N] were readily obtained by slow  
15 cooling of the solution in the presence of a slight excess of G3. This was the only complex  
16 that was analyzed by single crystal XRD. The unit cell of [K(G3)<sub>2</sub>][Tf<sub>2</sub>N] is shown in Figure  
17 3. The full crystallographic data can be found in the ESI (Table S5) and a close-up of the  
18 crystal structure in Figure S5.

19



1

2 **Figure 3.** View of the unit cell of the solvate complex  $[K(G3)_2][Tf_2N]$ . The disorder of the  
3  $Tf_2N^-$  anion is not shown. Purple, K; red, O; grey, C; white, H; yellow, S; green, F; cyan, N.

4

5  $[K(G3)_2][Tf_2N]$  crystallizes in the triclinic space group P-1. The asymmetric unit consists of a  
6  $K^+$  cation, two triglyme molecules and two halves of a  $Tf_2N^-$  anion. The full  $Tf_2N^-$  anion is  
7 generated by an inversion center. The first half of the  $Tf_2N^-$  anion is disordered and was  
8 refined over two positions. The second half was too disordered to be refined and instead, the  
9 solvent mask procedure was used for the refinement. The  $K^+$  cations are coordinated by eight  
10 oxygen atoms of two perpendicularly oriented triglyme ligands, leading to a total coordination  
11 number of eight (Figure S5). The  $Tf_2N^-$  anions are not coordinated and are strongly  
12 disordered. Therefore, the solvate structure of  $[K(G3)_2][Tf_2N]$  in the crystalline state can be  
13 classified as a SSIP-type solvate. This structure is similar to the crystal structure of  
14  $[Na(G3)_2][FSI]$ .<sup>15</sup> The  $K-O_{\text{glyme}}$  distances vary from 2.7627(15) Å to 2.8381(14) Å.  
15 Although the crystal structure of  $[K(G4)][Tf_2N]$  could not be determined, it might still be  
16 possible to estimate the structure on the basis of the existing literature. Mandai *et al.* have  
17 determined the crystal structure of several potassium salt-glyme solvate complexes with  
18 various anions such as  $Tf_2N^-$ , trifluoromethanesulfonate (OTf), hexafluorophosphate ( $PF_6^-$ )  
19 and perchlorate ( $ClO_4^-$ ).<sup>27,48</sup> According to the authors,  $K^+$  exhibits coordination numbers of 8  
20 to 10 in glymes. G4 is a pentadentate ligand which has five oxygen atoms available for



1 coordination. Therefore, one G4 ligand is not enough to saturate the first coordination shell of  
2  $\text{K}^+$  and the vacant coordination sites will most likely be occupied by oxygen atoms of the  
3  $\text{Tf}_2\text{N}^-$  anion. The solvate complex  $[\text{K}(\text{G}5)][\text{Tf}_2\text{N}]$  exhibits an AGG solvate structure, where  
4 the  $\text{K}^+$  cations are linked together one-dimensionally by bridging  $\text{Tf}_2\text{N}^-$  anions, so this is most  
5 likely also the case for  $[\text{K}(\text{G}4)][\text{Tf}_2\text{N}]$ . This was also evident from the Raman analysis of this  
6 complex (*vide infra*).

7 The melting point of the solvate complex  $[\text{K}(\text{G}4)_2][\text{Tf}_2\text{N}]$ , 19 °C, was too low for a single  
8 crystal XRD study. However, the crystal structure of  $[\text{K}(\text{G}4)_2][\text{PF}_6^-]$  was reported to be a  
9 SSIP-type solvate where  $\text{K}^+$  is coordinated by ten oxygen atoms of two G4 ligands. Similarly  
10 to  $\text{PF}_6^-$ ,  $\text{Tf}_2\text{N}^-$  is also a weakly coordinating anion and it is more bulky. Therefore the SSIP  
11 structure is also very likely for  $[\text{K}(\text{G}4)_2][\text{Tf}_2\text{N}]$  in the solid state.

12 In the solvate complexes  $[\text{K}(\text{G}1)_3][\text{Tf}_2\text{N}]$  and  $[\text{K}(\text{G}2)_2][\text{Tf}_2\text{N}]$ , there are only six glyme  
13 oxygen atoms available for coordination, so their structure will probably also be an AGG or  
14 CIP type in the solid state. In  $[\text{K}(\text{G}2)_3][\text{Tf}_2\text{N}]$ , nine glyme oxygen atoms are available, so this  
15 is possibly a SSIP type solvate complex. Unfortunately, it was not possible to analyze these  
16 complexes in the solid state by Raman spectroscopy, due to their low melting points.

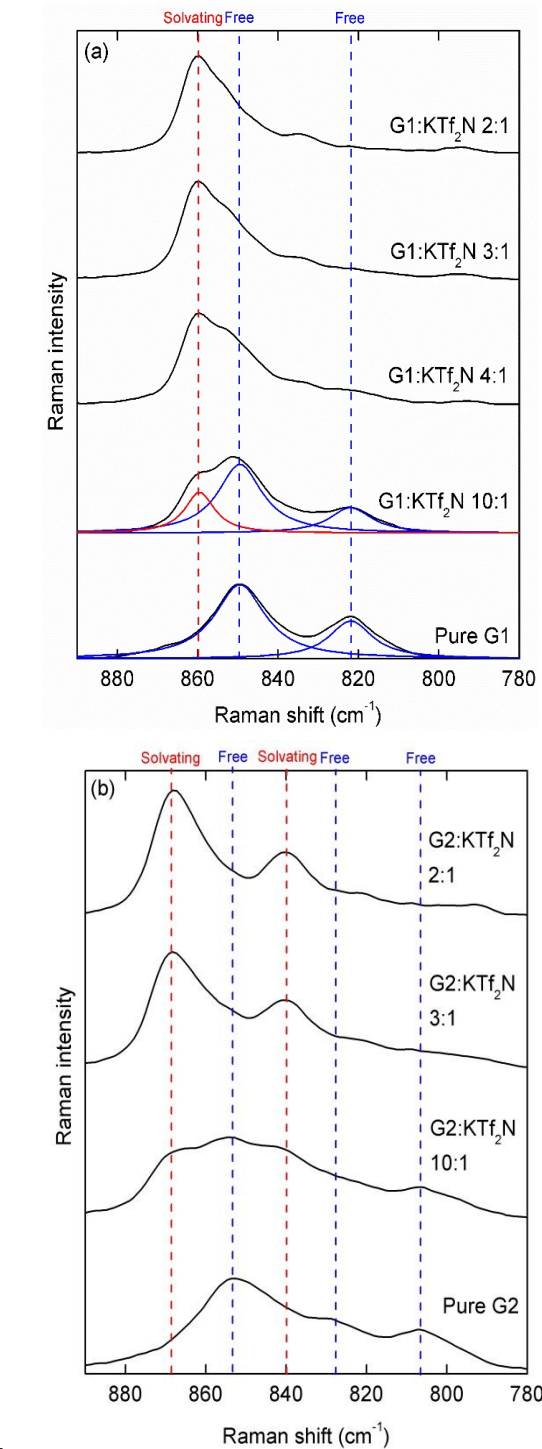
17 The solvation structures in liquid as well as solid glyme–alkali salt binary mixtures have been  
18 studied intensively by Raman spectroscopy.<sup>27,48,49</sup> Two regions of the Raman spectrum are of  
19 particular interest in our case of glyme– $\text{KTf}_2\text{N}$  binary mixtures. The first region is located in  
20 the range 780–900  $\text{cm}^{-1}$ , which corresponds to the coupled  $\text{CH}_2$  rocking ( $\text{r}(\text{CH}_2)$ ) and COC  
21 stretching ( $\text{v}(\text{COC})$ ) modes. When solvate complexes are formed between glyme ligands and  
22 an alkali cation, a new characteristic band is observed in this region of the Raman spectrum,  
23 shifted to higher wavenumbers. This band corresponds to the coupled  $\text{CH}_2$  rocking ( $\text{r}(\text{CH}_2)$ )  
24 and COC stretching ( $\text{v}(\text{COC})$ ) modes of coordinated glyme molecules, also known as the



1 “ring breathing mode”. Therefore, this band is a useful fingerprint mode to study solvation of [View Article Online](http://www.rsc.org/doi/10.1039/D5DT02781K)  
DOI: 10.1039/D5DT02781K

2 alkali salts in glymes. In order to characterize the solvation of  $\text{KTf}_2\text{N}$  in glymes, Raman  
3 spectra were recorded for several glyme: $\text{KTf}_2\text{N}$  molar ratios. The concentration dependence  
4 of the Raman spectra for the G1– $\text{KTf}_2\text{N}$  and G2– $\text{KTf}_2\text{N}$  binary mixtures in the range  
5 780–890  $\text{cm}^{-1}$  is shown in Figure 4.

6



1 **Figure 4.** Concentration dependence of the Raman spectra in the range 780–890 cm<sup>-1</sup> for (a)  
2 G1–KTf<sub>2</sub>N and (b) G2–KTf<sub>2</sub>N mixtures. The Raman spectra of the pure G1 and G2 are also  
3 included in the respective figures. The blue and red curves are peak fits produced by the  
4 deconvolution of the multipeaks, where the blue curves are fitted to bands characteristic of  
5 free glymes and the red curves to bands characteristic of solvating glymes.



1

View Article Online  
DOI: 10.1039/D5DT02781K

2 The multipeak in the Raman spectrum of pure monoglyme in this region can be deconvoluted  
3 into two bands at 822 and 850  $\text{cm}^{-1}$  which correspond to the coupled  $\text{r}(\text{CH}_2)/\nu(\text{COC})$  modes  
4 of free G1 molecules in different conformations.<sup>15</sup> In the spectrum of a 10:1 G1:KTf<sub>2</sub>N  
5 mixture, a third band is observed at 860  $\text{cm}^{-1}$ , indicating the presence of G1 molecules that  
6 are coordinated to potassium cations. This shift to higher wavenumbers is significantly  
7 smaller than for the case of G1–NaFSI mixtures (866  $\text{cm}^{-1}$ ), probably because the charge  
8 density of K<sup>+</sup> cations is lower than that of Na<sup>+</sup> cations, and therefore the interactions with the  
9 G1 solvent are weaker.<sup>15</sup> The two bands that are characteristic for free G1 molecules are also  
10 still present, since, at this ratio, G1 is present in a large excess compared to KTf<sub>2</sub>N. As the  
11 concentration of KTf<sub>2</sub>N in the binary mixtures is increased, the band at 860  $\text{cm}^{-1}$  becomes  
12 more intense, whereas the bands at 850 and 822  $\text{cm}^{-1}$  become less intense, which indicates  
13 that the amount of free G1 molecules in the mixtures decreases. Generally speaking with  
14 HCEs and SILs, the bands at 850 and 822  $\text{cm}^{-1}$  should completely disappear, indicating that  
15 almost no free G1 is present in the mixtures and practically all the available G1 is  
16 coordinated. However, judging from the large shoulder on the 860  $\text{cm}^{-1}$  band, this is not the  
17 case here. This means that even at a G1:KTf<sub>2</sub>N ratio of 2:1 there is still some uncoordinated  
18 G1 present, which is surprising and might be a consequence of the exceptionally weak G1–K<sup>+</sup>  
19 interactions and the poor chelate effect of G1. Besides the intense band at 860  $\text{cm}^{-1}$ , a second  
20 less intense band at approx. 835  $\text{cm}^{-1}$  is also observed. This can probably also be attributed to  
21 coordinated G1 molecules.

22 The Raman spectrum of pure diglyme is significantly more complex than that of monoglyme  
23 and it was not possible to produce a satisfactory multipeak fit in the 780–890  $\text{cm}^{-1}$  region.  
24 According to Johansson *et al.* the Raman spectrum of liquid diglyme is a combination of the  
25 individual spectra of a large number of different conformers that are in equilibrium with each

1 other.<sup>50</sup> Thus, deconvolution of this multipeak in only three bands would be a very simplified  
2 representation. However, three bands can be distinguished in the raw Raman spectrum at  
3 approx. 807, 828, and 852 cm<sup>-1</sup>, where the bands at 807 and 852 cm<sup>-1</sup> correspond to the *trans*  
4 and *gauche* conformations of the C–C bond in diglyme, respectively. The band at 807 cm<sup>-1</sup>  
5 corresponds to the coupled r(CH<sub>2</sub>)/tw(CH<sub>2</sub>) modes, and the band at 852 cm<sup>-1</sup> corresponds to  
6 the coupled r(CH<sub>2</sub>)/v(COC) modes of a free G2 molecule and both can be used as a  
7 fingerprint mode for solvation studies. In the spectrum of a 10:1 G2–KTf<sub>2</sub>N mixture, two new  
8 bands appear at 841 and 868 cm<sup>-1</sup> due to the coordination of G2 molecules to K<sup>+</sup> cations.  
9 Similarly to the G1–KTf<sub>2</sub>N mixtures, these bands become more intense as the KTf<sub>2</sub>N  
10 concentration increases, whereas the bands characteristic for free G2 become less intense. For  
11 the 2:1 G2–KTf<sub>2</sub>N mixture, only a slight shoulder can be observed on the 868 cm<sup>-1</sup> band,  
12 indicating that almost all of the available G2 solvent molecules are coordinated to K<sup>+</sup> cations.  
13 Judging from this behavior and the larger shift of the coordinated G2 band (868 cm<sup>-1</sup>)  
14 compared to uncoordinated band (852 cm<sup>-1</sup>), the solvation of K<sup>+</sup> cations in G2 is significantly  
15 stronger than in G1, which is expected according to the chelate effect. For the 3:1 mixture, the  
16 band at 852 cm<sup>-1</sup> can still barely be observed, hence in the liquid state, there is still a  
17 significant amount of free G2 present. This will also become evident from the coordination  
18 study of the Tf<sub>2</sub>N<sup>-</sup> anion (*vide infra*).  
19 The concentration dependance of the Raman spectra of G3–KTf<sub>2</sub>N mixtures in the range  
20 780–890 cm<sup>-1</sup> is largely analogous to G2–KTf<sub>2</sub>N mixtures (Figure S6). The multipeak  
21 produced by pure G3 consists of roughly three bands at approx. 807, 829 and 851 cm<sup>-1</sup>. Upon  
22 solvation of K<sup>+</sup> cations, *i.e.* for the 10:1 G3–KTf<sub>2</sub>N mixture, two new bands appear in the  
23 spectrum at approx. 840 and 868 cm<sup>-1</sup>. Interestingly, for the 2:1 mixture, *i.e.* the solid SSIP  
24 solvate complex [K(G3)<sub>2</sub>][Tf<sub>2</sub>N], the solvating band is shifted to even higher wavenumbers  
25 (872 cm<sup>-1</sup>). This was also observed for the sodium-containing solid solvate complex

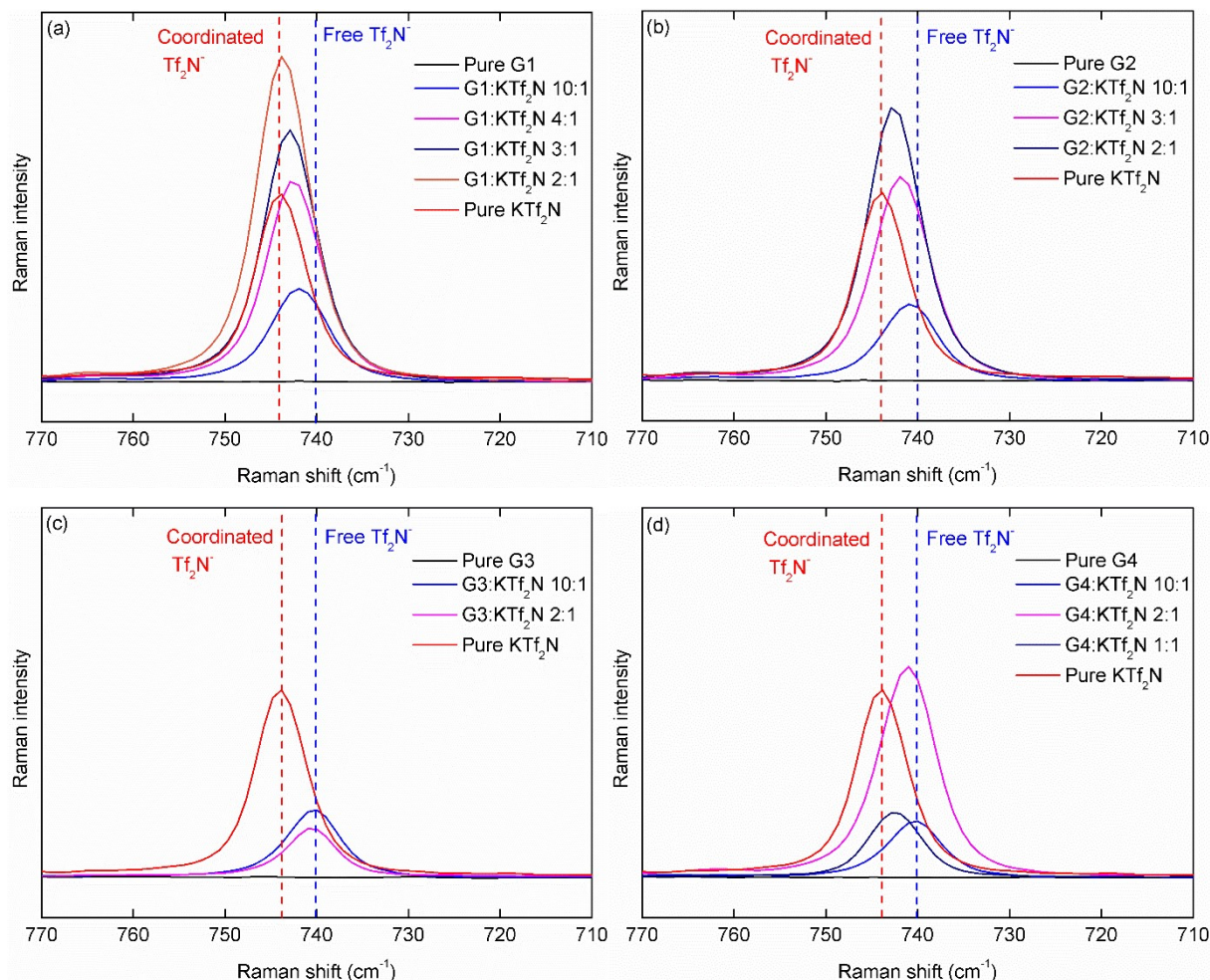
1 [Na(G3)<sub>2</sub>][FSI].<sup>15</sup> This indicates an even stronger glyme–K<sup>+</sup> interaction in the solid complex  
2 compared to the liquid solutions because the glyme chains are wrapped even more tightly  
3 around the K<sup>+</sup> cation. It should be noted that it was not possible to measure many other  
4 G3–KTf<sub>2</sub>N mixtures because crystals of [K(G3)<sub>2</sub>][Tf<sub>2</sub>N] started to precipitate out, leading to  
5 inhomogeneous mixtures.

6 The concentration dependance of the Raman spectra of G4–KTf<sub>2</sub>N mixtures in the range  
7 780–890 cm<sup>-1</sup> is again analogous (Figure S7). The spectrum of pure G4 in this region consists  
8 of roughly three bands at approx. 807, 829 and 851 cm<sup>-1</sup>. When KTf<sub>2</sub>N is added, two new  
9 bands at approx. 835 and 866 cm<sup>-1</sup> are observed, corresponding to solvating G4 molecules. In  
10 this case, the 866 cm<sup>-1</sup> band is not shifted to higher wavenumbers in the solid solvate complex  
11 [K(G4)][Tf<sub>2</sub>N], as was the case for [K(G3)<sub>2</sub>][Tf<sub>2</sub>N]. Interestingly, for the liquid 2:1  
12 G4–KTf<sub>2</sub>N mixture, *i.e.* the solvate complex [K(G4)<sub>2</sub>][Tf<sub>2</sub>N] (mp: 19 °C), there is still a  
13 noticeable band of free G4 present in the Raman spectrum. This would mean that, even  
14 though [K(G4)<sub>2</sub>][Tf<sub>2</sub>N] very likely has a SSIP structure in the solid state, upon melting some  
15 of the G4 ligands are desolvated from the K<sup>+</sup> cations. This is supported by the TGA data of  
16 this complex (*vide supra*), which showed relatively poor thermal stability for [K(G4)<sub>2</sub>][Tf<sub>2</sub>N].

17 The second region of interest for solvation studies of glyme–KTf<sub>2</sub>N binary mixtures is located  
18 in the range 710–770 cm<sup>-1</sup>. Here, the S–N stretching modes ( $\nu$ (SN)) of the Tf<sub>2</sub>N<sup>-</sup> anion are  
19 located, which are sensitive to its coordination environment. For a free (non-coordinating)  
20 Tf<sub>2</sub>N<sup>-</sup> anion, this band is located at approx. 740 cm<sup>-1</sup>.<sup>27</sup> On the other hand, in pure crystalline  
21 KTf<sub>2</sub>N, which has an AGG structure, this band is located at approx. 744 cm<sup>-1</sup>.<sup>51</sup> This shift is  
22 rather small but this can again be possibly explained by the low Lewis acidity of the K<sup>+</sup>  
23 cation. Thus, these bands can be used as fingerprint modes to assess the degree of ion pairing  
24 (*i.e.* CIP and AGG formation) in glyme–KTf<sub>2</sub>N binary mixtures. The concentration

1 dependence of the Raman spectra for G1–KTf<sub>2</sub>N, G2–KTf<sub>2</sub>N, G3–KTf<sub>2</sub>N, and G4–KTf<sub>2</sub>N  
2 binary mixtures in the range 690–770 cm<sup>−1</sup> is shown in Figure 5.

3



5 **Figure 5.** Concentration dependence of the Raman spectra in the range 690–770 cm<sup>−1</sup> for (a)  
6 G1–KTf<sub>2</sub>N, (b) G2–KTf<sub>2</sub>N, (c) G3–KTf<sub>2</sub>N, and (d) G4–KTf<sub>2</sub>N. G3–KTf<sub>2</sub>N 3:1 was an  
7 inhomogeneous mixture and was omitted from the plot.

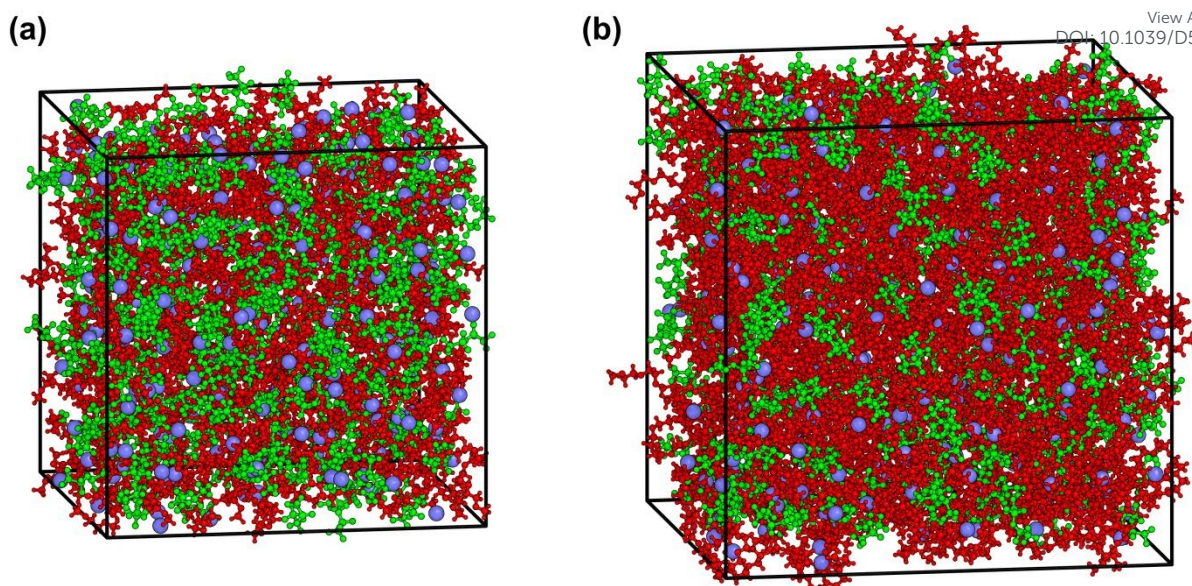
8

9 For all four systems, a dependence is observed between the  $\nu(\text{SN})$  band and the KTf<sub>2</sub>N  
10 concentration. Upon increasing the KTf<sub>2</sub>N concentration, the  $\nu(\text{SN})$  band shifts increasingly  
11 towards the 744 cm<sup>−1</sup> of pure crystalline KTf<sub>2</sub>N, indicating the formation of CIPs and AGGs

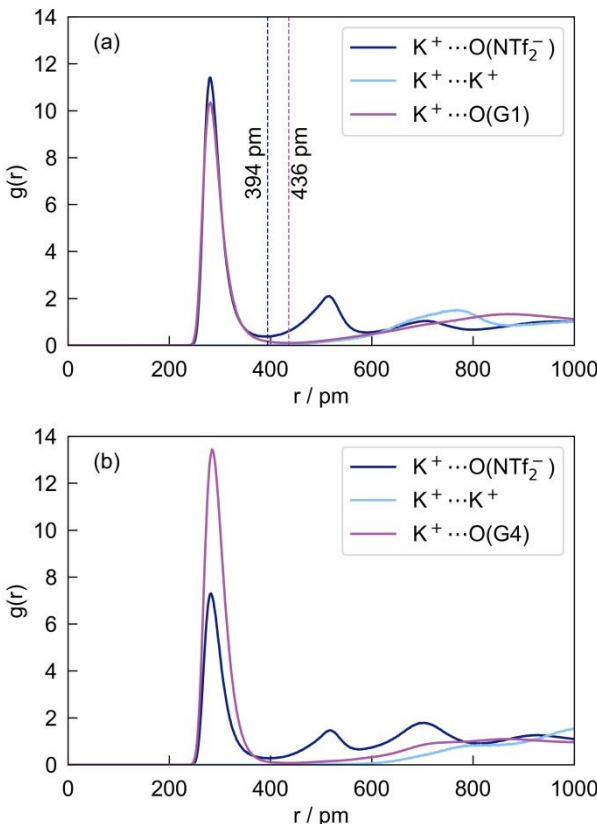
1 in the mixtures. When the different glyme systems are compared to each other, a trend is [View Article Online](#)  
DOI: 10.1039/D5DT02781K

2 observed. For the G1–KTf<sub>2</sub>N series of mixtures, the  $\nu(\text{SN})$  band is already shifted  
3 significantly towards higher wavenumbers even at the 10:1 G1:KTf<sub>2</sub>N ratio, meaning that  
4 even at this relatively dilute condition, CIPs and AGGs are already formed. For the  
5 G2–KTf<sub>2</sub>N series of mixtures, this is also the case but to a lesser extent than for the G1  
6 analogues. For the G3–KTf<sub>2</sub>N and G4–KTf<sub>2</sub>N series, the  $\nu(\text{SN})$  band is located at approx.  
7 740 cm<sup>-1</sup> at the 10:1 ratio, indicating that the KTf<sub>2</sub>N salt is fully dissociated into SSIPs at this  
8 concentration. For the 2:1 G3:KTf<sub>2</sub>N mixture, *i.e.* the solid SSIP solvate complex  
9 [K(G3)<sub>2</sub>][Tf<sub>2</sub>N], this band is not shifted to higher wavenumbers, which confirms the SSIP  
10 solvate structure of this complex which was revealed by single crystal XRD (*vide supra*). On  
11 the other hand, for the liquid 2:1 G4:KTf<sub>2</sub>N mixture, *i.e.* the solvate complex [K(G4)<sub>2</sub>][Tf<sub>2</sub>N]  
12 (mp: 19 °C), the  $\nu(\text{SN})$  band is shifted compared to the 740 cm<sup>-1</sup> line. This supports the  
13 cationic Raman spectra and TGA data that in the liquid state, the second G4 ligand is easily  
14 desolvated and is replaced by Tf<sub>2</sub>N<sup>-</sup> anions, leading to CIP and AGG formation. For the solid  
15 solvate complex [K(G4)][Tf<sub>2</sub>N], the band is noticeably shifted, so the solvate structure in the  
16 solid state is indeed probably a CIP or AGG type. This is expected since the five available  
17 ether oxygen atoms in G4 are not sufficient to fill the first coordination shell of K<sup>+</sup>. Therefore,  
18 Tf<sub>2</sub>N<sup>-</sup> anions have to fill in the open positions.

19 Molecular dynamics (MD) simulations were performed to investigate the cation's solvation  
20 sphere and further rationalize the experimental findings (Figure 6). The simulated systems  
21 comprise Gn–KTf<sub>2</sub>N mixtures with n = 1–4 at compositions of 4:1, 3:1, and 2:1. Radial  
22 distribution functions (RDFs) were calculated to gain insights into the cation's interactions  
23 with the different species in the system. For the ease of comparison with the solvent the  
24 discussion of the cation's interaction with the anion will be limited to the anion's oxygen  
25 atoms. The RDFs for the anion's center of mass can be found in the ESI (Figures S8 and S9).



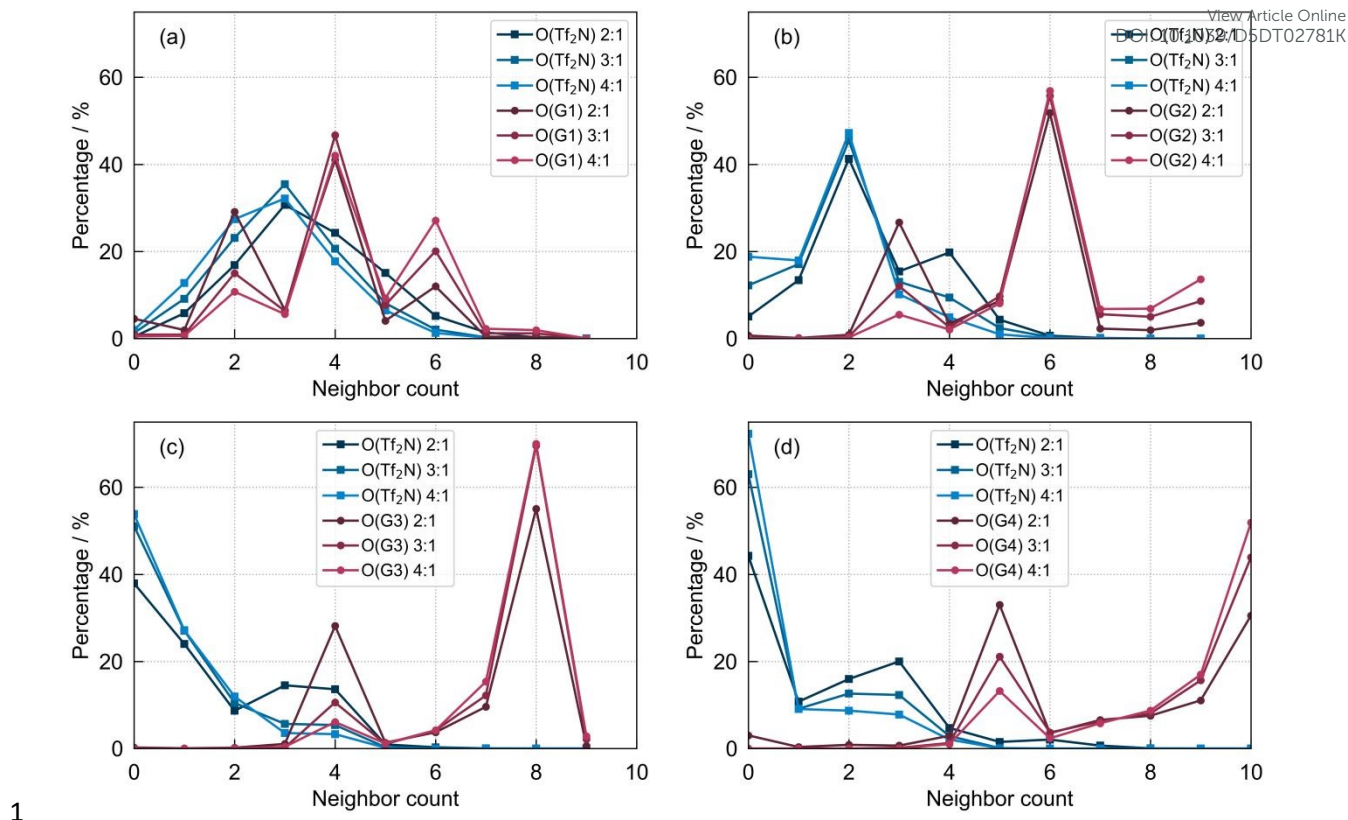
1

2 **Figure 6.** Simulation boxes of the (a) G1-KTf<sub>2</sub>N 2:1 system and (b) G4-KTf<sub>2</sub>N 2:1 system.3 Red: G1/G4, blue: K<sup>+</sup>, green: Tf<sub>2</sub>N<sup>-</sup>.5 **Figure 7.** Radial distribution functions (RDFs) of the K<sup>+</sup> cation interacting with other ions6 and the solvent in the 2:1 mixture of (a) G1-KTf<sub>2</sub>N and (b) G4-KTf<sub>2</sub>N.

1

View Article Online  
DOI: 10.1039/D5DT02781K

2 Figure 7 shows the RDFs for the cation's interactions with the oxygen atoms of the  $\text{Tf}_2\text{N}^-$   
3 anion and the glyme solvent as well as the interaction with other cations in the respective 2:1  
4 mixtures of G1– $\text{KTf}_2\text{N}$  and G4– $\text{KTf}_2\text{N}$ . The RDFs for the other simulated systems can be  
5 found in the ESI (Figures S8 and S9). Sharp peaks are observed in both systems for the  
6 cation's interaction with the oxygen atoms of the anion and solvent located at a distance of  
7 282 pm, indicating an ordered first coordination shell. In G1 the first peaks for the anion and  
8 solvent are similar in height and width, whereas in G4 the anion's peak is reduced compared  
9 to that of the solvent, as the anion is replaced in the cation's first solvation shell. At larger  
10 distances, two smaller peaks are observed for the anion's oxygen atom located at 515 pm and  
11 702 pm. These correspond to the non-coordinating oxygen atoms of a coordinating anion and  
12 an anion in the second solvation shell, respectively. In G4, the more distant peak gains  
13 intensity relative to the first two, indicating a shift from contact ion pairs to solvent separated  
14 ion pairs. No distinct peaks are observed in either system for the cation's interaction with the  
15 solvent's oxygen atoms at larger distances, indicating no ordered aggregation of solvent  
16 molecules around the cation beyond the first solvation shell. A small peak is observed in G1  
17 for the cation's interaction with other cations located at 770 pm, whereas no peak is observed  
18 in G4. This may indicate a tendency for the formation of aggregates in G1 and their absence  
19 in G4.



1 **Figure 8.** Neighbor count histogram for the cation's first solvation shell in (a) G1, (b) G2, (c)  
2 G3, and (d) G4. Lines are meant to guide the eye.

4

5 It is evident that while the average coordination sphere of the cation changes with the solvent,  
6 the formation of CIPs remains significant even in the stronger chelating G4. To gain deeper  
7 insight into the composition of the cation's first solvation shell, neighbor count analyses were  
8 performed. An oxygen atom is considered part of the first solvation shell if it is within 394 pm  
9 for the anion and 436 pm for the solvent, which corresponds to the location of the first  
10 minimum in their respective RDFs (Figure 7). By evaluating these conditions for every cation  
11 over the entire simulation trajectory, a histogram of the average number of cations  
12 coordinated by a given number of particles can be constructed. The obtained histograms are  
13 shown in Figure 8. In agreement with the RDFs, it is evident that the formation of CIPs  
14 remains significant in all systems regardless of composition. In G1 the amount of cations with

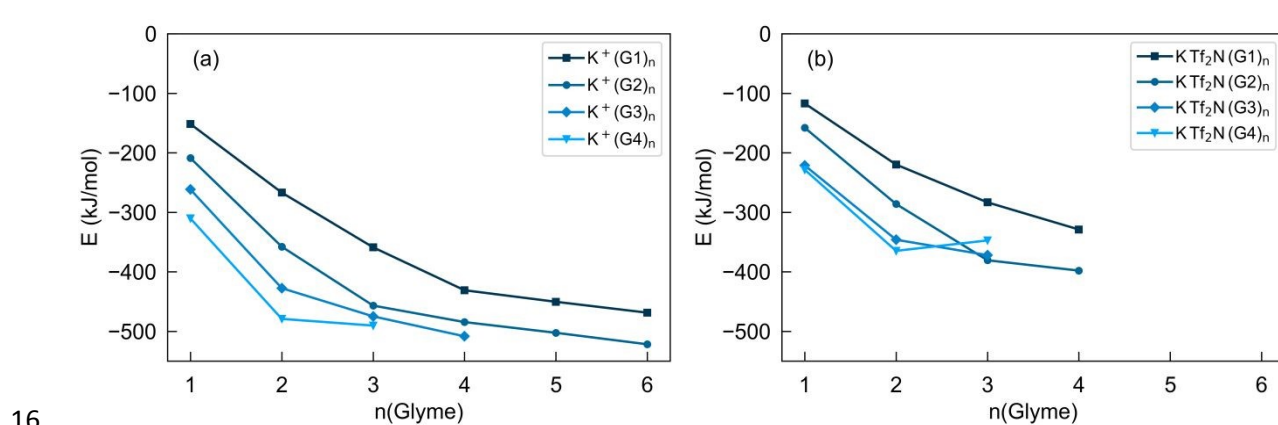


1 no direct contact to an anion's oxygen is <2% for all compositions. The number of fully solvated cations increases with both the glyme length and the amount of solvent, from 19% in G2-KTf<sub>2</sub>N 4:1 to 54% in G3-KTf<sub>2</sub>N 4:1 and 72% in G4-KTf<sub>2</sub>N 4:1. The solvent histograms show distinct peaks at neighbor counts corresponding to integer multiples of the number of oxygen atoms per solvent molecule, indicative of the chelate effect causing the solvent molecules to fully coordinate to a cation rather than being partly involved in its first solvation shell. Consequently, the most populated solvent oxygen neighbor counts increase with glyme length, from 4 in G1 to 6, 8, and 10 in G2, G3, and G4, respectively. In G1 and G2, a small but significant number of cations have neighbor counts of 6 or 9, respectively, corresponding to coordination by three solvent molecules. In contrast, coordination by more than two solvent molecules is not observed in G3 and G4. Counting both the anion and solvent oxygen atoms the total coordination number rises with both the glyme length and the amount of solvent from an average of 6.9 in G1-KTf<sub>2</sub>N 2:1 to 7.2 in G1-KTf<sub>2</sub>N 4:1 and 8.6 in G4-KTf<sub>2</sub>N 2:1.

14 These trends are broadly consistent with the experimentally observed Raman shifts. The v(SN) Raman band probes the local coordination environment of the Tf<sub>2</sub>N<sup>-</sup> anion. Therefore, to allow a direct comparison between the computationally obtained ion pair population and Raman trends, we calculated the fraction of anions bound in AGG structures (see Tables S7 – S14), defined as Tf<sub>2</sub>N<sup>-</sup> coordinated by two or more cations. At the most dilute simulated composition (4:1), this fraction decreases sharply with glyme length from 70% in G1 to 27% in G2, 7% in G3, and 3% in G4. This is well in agreement with the experimentally observed persistence of the v(SN) upshift in G1 but not in G3 and G4. Upon increasing salt concentration from 4:1 to 2:1, the amount of anions bound in AGG structures increases in all systems (e.g., from 3% to 26% in G4), consistent with the v(SN) shift toward the solid KTf<sub>2</sub>N limit. A plot of the Raman v(SN) peak position against the MD-derived AGG fraction (Figure S10) shows a strong qualitative correlation.



1 Figure 9(a) shows the cation binding energy as obtained from DFT calculations as a function  
 2 of the number of coordinating glyme molecules in the absence of the anion. The binding  
 3 energy of a single glyme molecule coordinating the cation increases from G1 to G4. Each  
 4 additional glyme molecule has a diminishing contribution to the total binding energy until the  
 5 cation's coordination sphere is saturated and the contribution of further molecules drops to  
 6  $<50$  kJ mol $^{-1}$ . As the number of oxygen atoms per coordinating glyme molecule increases,  
 7 saturation is reached after fewer molecules. Following the series G1, G2, and G3, the cation  
 8 can fit up to four, three, or two glyme molecules in its coordination shell, respectively.  
 9 Remarkably, two molecules of G4 may fully coordinate the cation. The binding energy of the  
 10 saturated cation lies in the range of 430 kJ mol $^{-1}$  to 480 kJ mol $^{-1}$  which is similar to the  
 11 isolated  $\text{KTf}_2\text{N}$  ion pair's binding energy of 441 kJ mol $^{-1}$ . Figure 9(b) shows the binding  
 12 energy in the presence of the anion. Similar trends as for the anion-free clusters are observed.  
 13 However, due to the sterical hindrance by the anion, the glyme molecules may not be able to  
 14 fully coordinate the cation and their binding energy is significantly reduced. This effect  
 15 increases with the number of glyme molecules as well as their size.



17 **Figure 9.** (a) Binding energy  $E_b(n) = E(\text{K}^+(\text{Glyme})_n) - E(\text{K}^+) - E((\text{Glyme})_n)$  of the  $\text{K}^+$  cation  
 18 coordinated by a number of  $n$  glyme molecules. (b) Binding energy  $E_b(n) = E(\text{KTf}_2\text{N}$   
 19  $(\text{Glyme})_n) - E(\text{KTf}_2\text{N}) - E((\text{Glyme})_n)$  of the  $\text{KTf}_2\text{N}$  ion pair coordinated by a number of  $n$   
 20 glyme molecules.



1

[View Article Online](#)  
DOI: 10.1039/D5DT02781K

2 Electrochemical stabilities were calculated for the different glymes and their complexes  
3 formed with the cation in the presence and absence of the anion. The obtained potentials  $U_{\text{red}}$   
4 and  $U_{\text{ox}}$  for reduction and oxidation of various species and complexes are listed in Table 2.  
5 For the glymes in their isolated form the  $U_{\text{red}}$  and  $U_{\text{ox}}$  shift towards more positive and more  
6 negative values, respectively, as the glyme length increases, implying a smaller  
7 electrochemical stability window for G4 compared to G1. When forming a complex with the  
8  $\text{K}^+$  cation, the reduction and oxidation potential shift towards more positive values.  
9 Remarkably, compared to the isolated glymes the trend of  $U_{\text{red}}$  is reversed as it shifts slightly  
10 towards more negative values with increasing glyme length. This trend also persists in the  
11 presence of the anion. The addition of the anion shifts all potentials towards more negative  
12 values. Notably, compared to the isolated ion pair  $U_{\text{red}}$  is reduced for the glyme complexes.  
13 When comparing the saturated complexes, as established from the previous DFT analysis,  
14  $U_{\text{red}}$  is similar for all glymes, whereas no clear trend is observed for  $U_{\text{ox}}$  which fluctuates with  
15 increasing glyme length.

16

1

**Table 2.** Calculated reduction ( $U_{\text{red}}$ ) and oxidation ( $U_{\text{ox}}$ ) potentials for the cation and its complexes with various species.

Complex/specie	$U_{\text{red}}$ (V)	$U_{\text{ox}}$ (V)
S		
$[\text{Tf}_2\text{N}]^-$	-0.4	5.3
$\text{KTf}_2\text{N}$	-0.5	6.3
G1	-2.5	5.8
G2	-2.4	5.7
G3	-2.4	5.7
G4	-2.4	5.7
$[\text{K}(\text{G1})]^+$	0.0	6.3
$[\text{K}(\text{G2})]^+$	-0.2	6.7
$[\text{K}(\text{G3})]^+$	-0.4	6.6
$[\text{K}(\text{G4})]^+$	-0.5	6.5
$[\text{K}(\text{G1})][\text{Tf}_2\text{N}]$	-0.7	5.7
$[\text{K}(\text{G2})][\text{Tf}_2\text{N}]$	-0.9	5.7
$[\text{K}(\text{G3})][\text{Tf}_2\text{N}]$	-1.0	5.6
$[\text{K}(\text{G4})][\text{Tf}_2\text{N}]$	-1.0	5.2
$[\text{K}(\text{G1})_4]^+$	-1.0	6.2
$[\text{K}(\text{G2})_3]^+$	-1.0	5.9
$[\text{K}(\text{G3})_2]^+$	-1.0	6.2
$[\text{K}(\text{G4})_2]^+$	-1.0	5.9

2

1 To summarize: the complexes with the general formula  $[K(L)_n][Tf_2N]$  ( $L = G1, G2, G3, or$  View Article Online  
DOI: 10.1039/D5DT02781K

2  $G4; n = 2, 3$  or  $4$ ) are low-melting solvate complexes between an ion ( $K^+$ ) and ligands

3 (glymes) in a certain stoichiometric ratio, thereby satisfying criteria 1, 3 and 4 for SILs, as

4 proposed by Mandai *et al.*<sup>49</sup> However, because of the weaker  $K^+$ -glyme interactions,

5 significant ion pairing occurs and the thermal stability is rather poor, not meeting criteria 2

6 and 5. This is especially the case for the complexes with shorter glyme ligands ( $G1$  and  $G2$ ).

7 Therefore,  $[K(G1)_2][Tf_2N]$  and  $[K(G2)_2][Tf_2N]$  are classified as “poor” SILs whereas

8  $[K(G3)_2][Tf_2N]$  and  $[K(G4)_2][Tf_2N]$  are more akin to “true” SILs, which is expected based on

9 the stronger chelating properties of the longer glyme ligands.

10 *Cycling of  $[K(G1)_2][Tf_2N]$  and  $[K(G2)_2][Tf_2N]$  on organic cathodes*

11 To be useful as a battery electrolyte, the electrochemical window of the electrolyte should be

12 wider than the operating potential window of the battery. Therefore, the electrochemical

13 window of  $[K(G1)_2][Tf_2N]$  and  $[K(G2)_2][Tf_2N]$  was determined by cyclic voltammetry with a

14 platinum working electrode (Figure 10). These two HCEs were selected for further

15 electrochemical studies since they exhibited behavior closest to that of SILs, albeit “poor”

16 SILs (*vide supra*), while also having an acceptable ionic conductivity.  $[K(G3)_2][Tf_2N]$  and

17  $[K(G4)][Tf_2N]$  are solid at room temperature and  $[K(G4)_2][Tf_2N]$  has a rather low ionic

18 conductivity, so they were omitted from testing. Any other mixture has significant amounts of

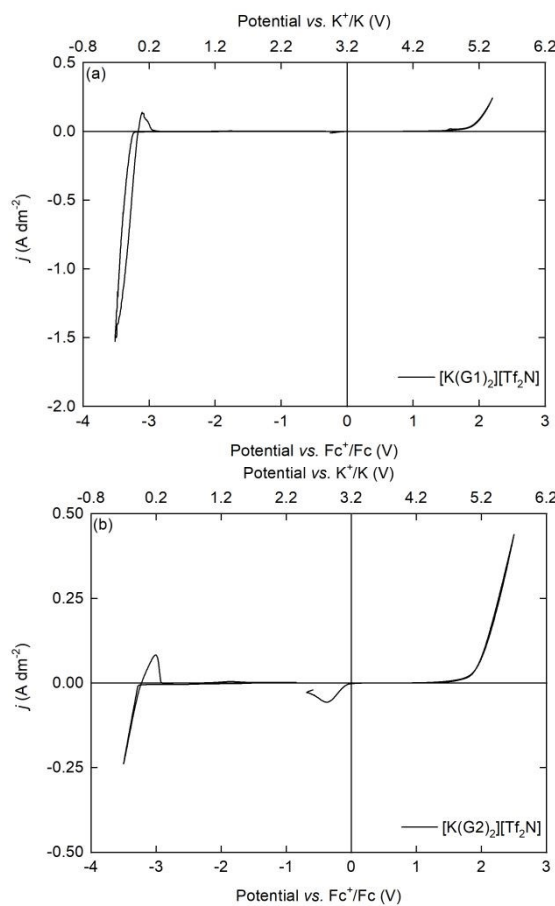
19 free glymes present so they cannot be categorized as HCEs or SILs. For the remainder of this

20 discussion, the general term HCEs will be used to refer to the poor SILs  $[K(G1)_2][Tf_2N]$  and

21  $[K(G2)_2][Tf_2N]$ .

22





1 **Figure 10.** Cyclic voltammograms of (a)  $[\text{K}(\text{G1})_2][\text{Tf}_2\text{N}]$  and (b)  $[\text{K}(\text{G2})_2][\text{Tf}_2\text{N}]$ , measured  
2 on a platinum working electrode with a scan rate of  $10 \text{ mV s}^{-1}$ . The counter electrode was  
3 platinum and the reference electrode was a platinum wire submerged in a solution of  
4 ferrocene (Fc) and ferrocenium hexafluorophosphate ( $\text{FcPF}_6$ ) ( $5 \text{ mmol L}^{-1}$  each) in  
5  $[\text{BMP}][\text{Tf}_2\text{N}]$ , contained inside a fritted glass tube (referred to as  $\text{Fc}^+/\text{Fc}$ ). The threshold for  
6 determination of the electrochemical window was 1% of the maximum potassium plating  
7 current density.

9  
10 For both HCEs, the cathodic limit corresponds to the deposition of potassium metal which  
11 occurs at a potential of  $-3.3 \text{ V}$  vs.  $\text{Fc}^+/\text{Fc}$ , which should correspond to approx.  $-0.1 \text{ V}$  vs.  
12  $\text{K}^+/\text{K}$ , considering that the electrodeposition of alkali metals is usually characterized by small  
13 overpotential. This is evidenced by the sudden negative increase in current density at this

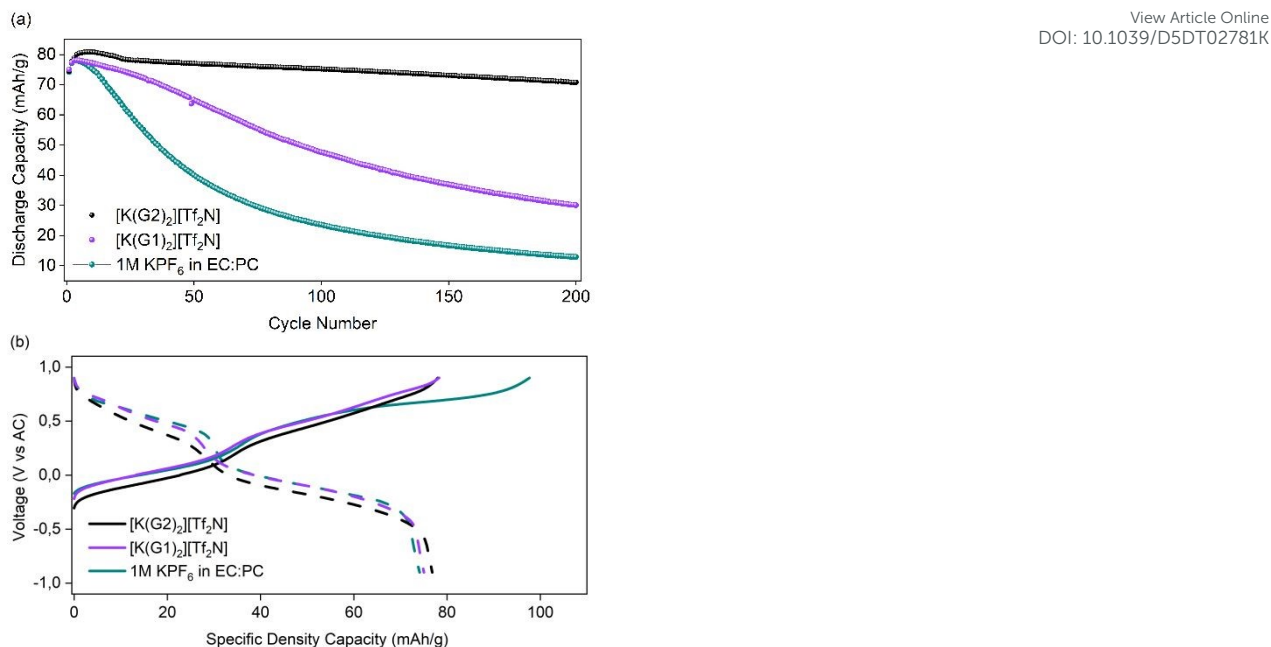
1 potential in the forward cathodic scan, and the corresponding stripping peak in the backwards  
2 scan. Judging from the size of the stripping peak in relation to the potassium electrodeposition  
3 current density, the deposition/stripping of potassium metal is clearly not very reversible. The  
4 observed Coulombic efficiency for potassium deposition/stripping was 4% for  
5  $[K(G1)_2][Tf_2N]$  and 28% for  $[K(G2)_2][Tf_2N]$ . Due to the high reactivity of potassium metal  
6 and its tendency to deposit dendritically at these high current densities, most of the deposit  
7 reacts with electrolyte components or gets lost from the working electrode as “dead”  
8 potassium. The anodic limit of the HCEs is around +1.7 V vs.  $Fe^{+}/Fe$  (or +4.9 V vs.  $K^{+}/K$ ) and  
9 corresponds to the decomposition of the ligands. Overall, all of the HCEs have an  
10 electrochemical window of approximately 5.0 V.

11 Since the electrodes used in the cycling experiments can also have a significant influence on  
12 the limiting potentials of the electrochemical window, the voltage range was chosen well  
13 within the determined boundaries (-1.0 V to +1.0 V vs. activated carbon (AC), which is about  
14 +2.0 V to +4.0 V vs.  $K^{+}/K$ ). For the galvanostatic cycling experiments, because of the high  
15 reactivity of potassium metal with the electrolyte, activated capacitive carbon (AC) was  
16 chosen as the counter/reference electrode instead of potassium metal. For the cathode  
17 (working electrode) material, the organic coordination polymer  
18  $K_2-Co$ –benzene–1,2,4,5–tetra-methylsulfonamide ( $K_2-Co-PTtSA$ ) was chosen which is  
19 reported elsewhere.<sup>32</sup>  $K_2-Co-PTtSA$  is, to date, the first and only reported cathode material  
20 synthesized directly in its reduced state, meaning that it is intrinsically potassium-containing.  
21 As such, it can operate as a cathode in a manner analogous to conventional lithium-ion battery  
22 cathodes. However, this system also presents several limitations. Although its electrical  
23 conductivity is relatively high for an organic battery material, it remains limited (approx.  
24  $10^{-7}$  S/cm). Consequently, a large fraction of conductive carbon additives (typically 20 –  
25 10 wt. %) is required in the electrode composite, significantly reducing the practical capacity



1 of the cathode. In addition, as a coordination polymer, the interactions between the organic  
2 ligand and the inorganic metal centers, while strong, are generally weaker than those found in  
3 fully inorganic materials. As a result, the choice of electrolyte becomes critical, as it directly  
4 governs the solubility of the coordination polymer. Excessive solubility in the electrolyte  
5 leads to rapid capacity fading and severely compromises the cycle life of the battery.  
6 Therefore, careful electrolyte design is essential to ensure sufficient ionic conductivity while  
7 simultaneously mitigating cathode dissolution, thereby enabling stable long-term  
8 electrochemical performance. In this regard,  $[K(G1)_2][Tf_2N]$  and  $[K(G2)_2][Tf_2N]$  are  
9 promising electrolytes to pair with  $K_2\text{--Co--PTtSA}$  because nearly all the glyme molecules are  
10 coordinated to  $K^+$  cations and are therefore less available to dissolve the cathode material,  
11 potentially improving the capacity retention. Besides  $[K(G1)_2][Tf_2N]$  and  $[K(G2)_2][Tf_2N]$ , an  
12 electrolyte consisting of  $1 \text{ mol L}^{-1} KPF_6$  in ethylene carbonate (EC):propylene carbonate (PC)  
13 was chosen as a standard reference electrolyte to compare the HCEs to. The galvanostatic  
14 cycling results for 200 cycles at a cycling rate of C/10 are depicted in Figure 11.

15



1 **Figure 11.** Cycling performance of  $\text{K}_2\text{-Co-PTtSA}$  cathodes in  $[\text{K}(\text{G}1)_2]\text{[Tf}_2\text{N}]$ ,  
2  $[\text{K}(\text{G}2)_2]\text{[Tf}_2\text{N}]$ , and 1 mol  $\text{L}^{-1}$   $\text{KPF}_6$  in EC:PC at a cycling rate of C/10. (a) Discharge  
3 capacity *vs.* cycle number over 200 cycles and (b) first cycle charge/discharge profiles for  
4 each electrolyte.

5

6  
7 Upon comparing the three different electrolyte systems, some significant differences can be  
8 observed (Figure 11a). In the first cycle, the specific discharge capacity is almost equal for all  
9 three electrolytes at approx.  $77 \text{ mAh g}^{-1}$ . However, for the 1 mol  $\text{L}^{-1}$   $\text{KPF}_6$  in EC:PC  
10 electrolyte, a fast capacity fade is observed over 200 cycles to a final specific discharge  
11 capacity of approx.  $15 \text{ mAh g}^{-1}$ . For the  $[\text{K}(\text{G}1)_2]\text{[Tf}_2\text{N}]$  electrolyte, capacity fading is also  
12 observed but at a much slower rate, with a final specific discharge capacity of approx.  
13 30  $\text{mAh g}^{-1}$  after 200 cycles. On the other hand, the specific discharge capacity of the cell  
14 with the  $[\text{K}(\text{G}2)_2]\text{[Tf}_2\text{N}]$  even slightly increases in the first ten cycles, and then remains  
15 remarkably stable to a final value of approx.  $70 \text{ mAh g}^{-1}$ . In the charge/discharge profiles, it  
16 can be observed that although the discharge capacity in the three electrolytes is almost equal,

1 the charge capacity is in fact significantly higher for the reference electrolyte 1 mol L<sup>-1</sup> KPF<sub>6</sub> in EC:PC (Figure 11b). Thus, the Coulombic efficiency is lower for 1 mol L<sup>-1</sup> KPF<sub>6</sub> in EC:PC (approx. 93%) compared to [K(G1)<sub>2</sub>][Tf<sub>2</sub>N] and [K(G2)<sub>2</sub>][Tf<sub>2</sub>N] (almost 100%). As mentioned above, this behavior could be possibly explained by a lower solubility of the cathode active material in [K(G1)<sub>2</sub>][Tf<sub>2</sub>N] and [K(G2)<sub>2</sub>][Tf<sub>2</sub>N] compared to the EC:PC electrolyte, or by a higher degree of irreversible side reactions in the latter electrolyte. To complement this discussion, a qualitative solubility test was performed by dispersing 10 mg of pristine K<sub>2</sub>–Co–PTtSA in 2 mL of the corresponding electrolytes, followed by sonication for 10 minutes. After 24 h, the suspensions were filtered, and the resulting filtrates are shown in Figure S11. As observed, the EC:PC-based electrolyte exhibits a markedly darker coloration compared to [K(G1)<sub>2</sub>][Tf<sub>2</sub>N], which itself is darker than [K(G2)<sub>2</sub>][Tf<sub>2</sub>N]. The pink coloration, characteristic of the dissolved PTtSA ligand, indicates a higher degree of coordination polymer dissolution in the EC:PC-based electrolyte, followed by [K(G1)<sub>2</sub>][Tf<sub>2</sub>N], and the lowest solubility in [K(G2)<sub>2</sub>][Tf<sub>2</sub>N]. This qualitative trend in solubility correlates well with the electrochemical results and provides a plausible explanation for the superior capacity retention observed with [K(G2)<sub>2</sub>][Tf<sub>2</sub>N], compared to [K(G1)<sub>2</sub>][Tf<sub>2</sub>N] and the EC:PC-based standard electrolyte. Secondly, as reported by Hosaka *et al.*, G2-based HCEs exhibit a significantly higher oxidative stability than G1-based HCEs, which also contributes to the higher observed stability of [K(G2)<sub>2</sub>][Tf<sub>2</sub>N].<sup>25</sup> Secondly, the rate performance of K<sub>2</sub>–Co–PTtSA was investigated in the three electrolyte systems (Figure 12).

22

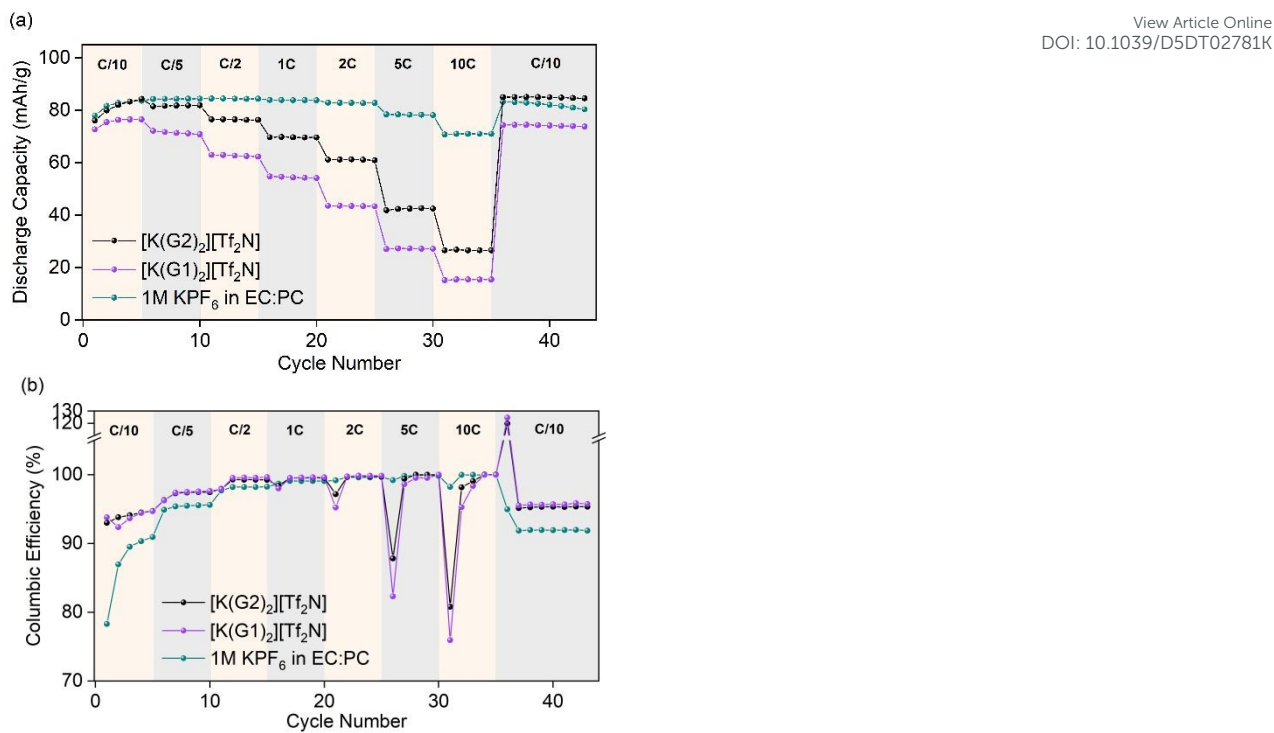


**Figure 12.** Rate performance of  $\text{K}_2\text{-Co-PTtSA}$  cathodes in  $[\text{K}(\text{G}1)_2]\text{[Tf}_2\text{N}]$ ,  $[\text{K}(\text{G}2)_2]\text{[Tf}_2\text{N}]$ , and  $1\text{ mol L}^{-1} \text{KPF}_6$  in EC:PC at cycling rates ranging from C/10 to 10C. (a) Specific discharge capacity *vs.* cycle number and (b) Coulombic efficiency *vs.* cycle number.

When comparing the rate performance of  $\text{K}_2\text{-Co-PTtSA}$  cathodes in the three electrolytes, some significant differences can be observed here as well (Figure 12a). For  $1\text{ mol L}^{-1} \text{KPF}_6$  in EC:PC, the rate performance is relatively good, as the achieved specific discharge capacity remains around  $81\text{ mAh g}^{-1}$  up to a cycling rate of 2C. Only at 5C and 10C, the specific discharge capacity is slightly decreased. However, for  $[\text{K}(\text{G}2)_2]\text{[Tf}_2\text{N}]$  and especially  $[\text{K}(\text{G}1)_2]\text{[Tf}_2\text{N}]$ , the rate performance is significantly worse, as the specific discharge capacity already decreases at a cycling rate of C/5. At 10C, the achieved specific discharge capacity is only approx.  $25\text{ mAh g}^{-1}$  for  $[\text{K}(\text{G}2)_2]\text{[Tf}_2\text{N}]$  and approx.  $15\text{ mAh g}^{-1}$  for  $[\text{K}(\text{G}1)_2]\text{[Tf}_2\text{N}]$ . This behavior can possibly be explained by the higher viscosity and lower ionic conductivity of the HCEs compared to the reference electrolyte. Furthermore, these electrolyte properties

1 are also strongly linked to other kinetic limitations, including charge-transfer resistance at the  
2 electrode–electrolyte interface and mass transport within the porous electrode. As the  
3 electrolyte ionic conductivity decreases and viscosity increases, ion mobility is reduced,  
4 leading to the development of steeper concentration gradients under high current densities.  
5 This not only slows interfacial charge-transfer kinetics, but also imposes severe mass-  
6 transport limitations, particularly within the electrolyte-filled pores of the composite  
7 electrode. In such conditions, the replenishment of  $K^+$  cations at the active material surface  
8 becomes rate-limiting, resulting in increased polarization and diminished rate capability.  
9 However, even though  $[K(G1)_2][Tf_2N]$  is less viscous and more conductive than  
10  $[K(G2)_2][Tf_2N]$ , its rate performance is actually worse, so this cannot be the only reason.  
11 Another factor that can contribute to charge-transfer limitations is the possible formation of a  
12 cathode–electrolyte interface (CEI) through side reactions of the charged cathode surface and  
13 electrolyte components. However, analysis of the CEI on this novel organic cathode material  
14 is very challenging and was outside the scope of this work. Looking at the Coulombic  
15 efficiency, the two HCEs consistently achieve higher values than the reference electrolyte  
16 (Figure 12b). Therefore, it can be concluded that the HCEs outperform the reference  
17 electrolyte in terms of long-term stability, but are outperformed in terms of rate performance.  
18 The rate performance of the HCEs can be possibly improved by using them to prepare  
19 localized high concentration electrolytes (LHCEs), which would increase the ionic  
20 conductivity significantly but keep the unique solvation structures of HCEs.<sup>26</sup> However, this  
21 was outside the scope of present work.  
22  
23  
24

## 1 Conclusion

2 Complexes with the general formula  $[K(L)_n][Tf_2N]$  ( $L = G1, G2, G3, \text{ or } G4; n = 2, 3 \text{ or } 4$ )  
3 were prepared and characterized. These complexes are classified as HCEs owing to their high  
4 concentration of  $KTf_2N$ . They were subsequently systematically investigated to see if they  
5 could also be classified as SILs, according to the criteria proposed by Mandai *et al.* Many of  
6 the HCEs are liquid at room temperature and have a reasonably low viscosity, making them  
7 potential candidates for use as electrolytes in KIBs. Their volatility, although reduced  
8 compared to pure glymes, was still high, especially for the G1 and G2 HCEs. The solvation  
9 structure of the HCEs was extensively studied by single crystal XRD and Raman  
10 spectroscopy, supported by molecular dynamics studies and DFT calculations. This revealed  
11 that a significant amount of ion pairing and aggregate formation occurred for all the tested  
12 HCEs. For the G1 and G2 HCEs this even occurred at relatively dilute concentrations.  
13 Therefore, the HCEs must be classified as “poor” SILs, since they lack some of the proposed  
14 criteria for “true” SILs. Despite this, the electrolytes  $[K(G1)_2][Tf_2N]$  and  $[K(G2)_2][Tf_2N]$  still  
15 exhibited acceptable conductivity so they were selected for a proof-of-concept galvanostatic  
16 cycling study on the organic cathode material  $K_2\text{--Co--PTtSA}$ . These two HCEs showed  
17 improved long term cycling stability (less capacity fading and higher Coulombic efficiency)  
18 compared to a standard reference electrolyte consisting of  $1 \text{ mol L}^{-1} KPF_6$  in EC:PC, but a  
19 worse rate performance due to the high viscosity.

20

**1 Electronic Supplementary Information (ESI)**

2 Conductivity, viscosity, density and potassium concentration of glyme–KTf<sub>2</sub>N electrolytes  
3 (Table S1–S4), crystallographic data of [K(G3)<sub>2</sub>][Tf<sub>2</sub>N] (Table S5), Molecular Dynamics  
4 parameters of various glyme–KTf<sub>2</sub>N systems (Table S6), population analysis of AGG  
5 structures in various glyme–KTf<sub>2</sub>N systems (Tables S7–S14), dynamic TGA curves of  
6 glyme–KTf<sub>2</sub>N complexes (Figure S1–S4), close-up of the crystal structure of [K(G3)<sub>2</sub>][Tf<sub>2</sub>N]  
7 (Figure S5), Raman spectra of G3–KTf<sub>2</sub>N and G4–KTf<sub>2</sub>N systems in the range 890–780 cm<sup>−1</sup>  
8 (Figure S6–S7), RDFs of K<sup>+</sup> interacting with different moieties in glyme–KTf<sub>2</sub>N systems at  
9 different ratios (Figure S8–S9), correlation graph of the Raman  $\nu$ (SN) peak position with the  
10 fraction of Tf<sub>2</sub>N<sup>−</sup> anions bound in AGG structures as obtained from MD (Figure S10),  
11 solubility test of pure K<sub>2</sub>–Co–PTtSA in the different used electrolytes (Figure S11).

**12 Acknowledgements**

13 This project (EOS 40007515) has received funding from the FWO and F.R.S.-FNRS under  
14 the Excellence of Science (EOS) programme.

15

**16 Conflict of interest**

17 There are no conflicts to declare

18

19

1 **References**View Article Online  
DOI: 10.1039/D5DT02781K

2

3 1. N. Yabuuchi, K. Kubota, M. Dahbi and S. Komaba, *Chem. Rev.*, 2014, **114**,  
4 11636–11682, DOI: 10.1021/cr500192f.

5 2. J. Muldoon, C. B. Bucur and T. Gregory, *Chem. Rev.*, 2014, **114**, 11683–11720, DOI:  
6 10.1021/cr500049y.

7 3. T. Hosaka, K. Kubota, A. S. Hameed and S. Komaba, *Chem. Rev.*, 2020, **120**, 6358–  
8 6466, DOI: 10.1021/acs.chemrev.9b00463.

9 4. J. Sun, Y. Du, Y. Liu, D. Yan, X. Li, D. H. Kim, Z. Lin and X. Zhou, *Chem. Soc. Rev.*,  
10 2025, **54**, 2543–2594, DOI: 10.1039/d4cs00845f.

11 5. S. Komaba, T. Hasegawa, M. Dahbi and K. Kubota, *Electrochem. Commun.*, 2015, **60**,  
12 172–175, DOI: 10.1016/j.elecom.2015.09.002.

13 6. K. Kubota, M. Dahbi, T. Hosaka, S. Kumakura and S. Komaba, *Chem. Rec.*, 2018, **18**,  
14 459–479, DOI: 10.1002/tcr.201700057.

15 7. A. Eftekhari, *J. Power Sources*, 2004, **126**, 221–228, DOI:  
16 10.1016/j.jpowsour.2003.08.007.

17 8. M. Okoshi, Y. Yamada, S. Komaba, A. Yamada and H. Nakai, *J. Electrochem Soc.*,  
18 2017, **164**, A54–A60, DOI: 10.1149/2.0211702jes.

19 9. M. Morita, T. Shibata, N. Yoshimoto and M. Ishikawa, *Electrochim. Acta*, 2002, **47**,  
20 2787–2793, DOI: 10.1016/S0013-4686(02)00164-0.

21 10. X. Bie, K. Kubota, T. Hosaka, K. Chihara and S. Komaba, *J. Mater. Chem. A*, 2017, **5**,  
22 4325–4330, DOI: 10.1039/c7ta00220c.

23 11. C. Zhang, Y. Xu, M. Zhou, L. Liang, H. Dong, M. Wu, Y. Yang and Y. Lei, *Adv.*  
24 *Funct. Mater.*, 2017, **27**, 1604307, DOI: 10.1002/adfm.201604307.

1 12. J. Liao, Q. Hu, Y. Yu, H. Wang, Z. Tang, Z. Wen and C. Chen, *J. Mater. Chem. A*, 2017, **5**, 19017–19024, DOI: 10.1039/C7TA05460B.

2 13. Z. Jian, W. Luo and X. Ji, *J. Am. Chem. Soc.*, 2015, **137**, 11566–11569, DOI: 10.1021/jacs.5b06809.

3 14. G. Vanhoutte, N. R. Brooks, S. Schaltin, B. Opperdoes, L. van Meervelt, J.-P. Locquet, P. M. Vereecken, J. Fransaer and K. Binnemans, *J. Phys. Chem. C*, 2014, **118**, 20152–20162, DOI: 10.1021/jp505479x.

4 15. P. Geysens, V. Shankar Rangasamy, S. Thayumanasundaram, K. Robeyns, L. van Meervelt, J.-P. Locquet, J. Fransaer and K. Binnemans, *J. Phys. Chem. B*, 2018, **122**, 275–289, DOI: 10.1021/acs.jpcb.7b10158.

5 16. P. Geysens, J. Fransaer and K. Binnemans, *RSC Adv.*, 2020, **10**, 42021–42029, DOI: 10.1039/d0ra08187f.

6 17. Y. Yamada and A. Yamada, *J. Electrochem. Soc.*, 2015, **162**, A2406–A2423, DOI: 10.1149/2.0041514jes.

7 18. Y. Yamada, K. Furukawa, K. Sodeyama, K. Kikuchi, M. Yaegashi, Y. Tateyama and A. Yamada, *J. Am. Chem. Soc.*, 2014, **136**, 5039–5046, DOI: 10.1021/ja412807w.

8 19. Y. Yamada, K. Usui, C. H. Chiang, K. Kikuchi, K. Furukawa and A. Yamada, *ACS Appl. Mater. Interfaces*, 2014, **6**, 10892–10899, DOI: 10.1021/am5001163.

9 20. M. Nie, D. P. Abraham, D. M. Seo, Y. Chen, A. Bose and B. L. Lucht, *J. Phys. Chem. C*, 2013, **117**, 25381–25389, DOI: 10.1021/jp409765w.

10 21. Q. Feng, J. Jiang, S. Li, G. Zhou, X. Kong, Y. Chen, Q. Zhuang and Z. Ju, *Small*, 2025, **21**, 2406506, DOI: 10.1002/smll.202406506.

11 22. Z. Yuan, J. Liao, L. Song, A. Chen, J. Su, J. Wang and X. Zhou, *Angew. Chem. Int. Ed.*, 2025, **64**, e202415923, DOI: 10.1002/anie.202415923.

1 23. N. Xiao, W. D. McCulloch and Y. Wu, *J. Am. Chem. Soc.*, 2017, **139**, 9475–9478. View Article Online  
DOI: 10.1039/D5DT02781K

2 DOI: 10.1021/jacs.7b04945.

3 24. T. Hosaka, K. Kubota, H. Kojima and S. Komaba, *Chem. Commun.*, 2018, **54**,

4 8387–8390, DOI: 10.1039/c8cc04433c.

5 25. T. Hosaka, T. Matsuyama, K. Kubota, R. Tatara and S. Komaba, *J. Mater. Chem. A*,

6 2020, **8**, 23766–23771, DOI: 10.1039/d0ta08851j.

7 26. W. Xu, H. Wang, Y. Gao, Y. Wie, H. Zhang, C. Gao, F. Kang and D. Zhai, *Energy*

8 *Adv.*, 2022, **1**, 191–196, DOI: 10.1039/d2ya00015f.

9 27. T. Mandai, S. Tsuzuki, K. Ueno, K. Dokko and M. Watanabe, *Phys. Chem. Chem.*

10 *Phys.*, 2015, **17**, 2838–2849, DOI: 10.1039/c4cp05017g.

11 28. G. Zeng, S. Xiong, Y. Qian, L. Ci and J. Feng, *J. Electrochem. Soc.*, 2019, **166**,

12 A1217–A1222, DOI: 10.1149/2.1171906jes.

13 29. O. V. Dolomanov, L. J. Bourhis, R. J. Gildea, J. A. K. Howard and H. Puschmann, *J.*

14 *Appl. Cryst.*, 2009, **42**, 339–341, DOI: 10.1107/S0021889808042726.

15 30. G. M. Sheldrick, *Acta Cryst.*, 2015, **A71**, 3–8, DOI: 10.1107/S2053273314026370.

16 31. G. M. Sheldrick, *Acta Cryst.*, 2015, **C71**, 3–8, DOI: 10.1107/S2053273314026370.

17 32. J. Wang, X. Guo, P. Apostol, X. Liu, K. Robeyns, L. Gence, C. Morari, J.-F. Gohy

18 and A. Vlad, *Energy Environ. Sci.*, 2022, **15**, 3923–3932, DOI: 10.1039/d2ee00566b.

19 33. A. P. Thompson, H. M. Aktulgä, R. Berger, D. S. Bolintineanu, W. M. Brown, P. S.

20 Crozier, P. J. in't Veld, A. Kohlmeyer, S. G. Moore, T. D. Nguyen, *Comput. Phys.*

21 *Commun.*, 2022, **271**, 108171, DOI: 10.1016/j.cpc.2021.108171.

22 34. W. L. Jorgensen, D. S. Maxwell, J. Tirado-Rives, *J. Am. Chem. Soc.*, 1996, **118**,

23 11225–11236, DOI: 10.1021/ja9621760.

1 35. K. P. Jensen, W. L. Jorgensen, *J. Chem. Theory Comput.*, 2006, **2**, 1499–1509, DOI: [10.1039/D5DT02781K](https://doi.org/10.1039/D5DT02781K)

2 10.1021/ct600252r.

3 36. J. E. Lennard-Jones, *Proc. Phys. Soc.*, 1931, **43**, 461, DOI: [10.1088/0959-5309/43/5/301](https://doi.org/10.1088/0959-5309/43/5/301).

4 37. L. Martínez, R. Andrade, E. G. Birgin, J. M. Martínez, *J. Comput. Chem.*, 2009, **30**,  
2157–2164, DOI: [10.1002/jcc.21224](https://doi.org/10.1002/jcc.21224).

5 38. S. Nosé, *J. Phys. Condens. Matter*, 1990, **2**, SA115, DOI: [10.1088/0953-8984/2/S/013](https://doi.org/10.1088/0953-8984/2/S/013).

6 39. W. G. Hoover, H. A. Posch, B. L. Holian, M. J. Gillan, M. Mareschal, C. Massobrio,  
*Mol. Simul.*, 1987, **1**, 79–86, DOI: [10.1080/08927028708080932](https://doi.org/10.1080/08927028708080932).

7 40. F. Neese, F. Wennmohs, U. Becker, C. Riplinger, *J. Chem. Phys.*, 2020, **152**, DOI:  
10.1063/5.0004608.

8 41. S. Grimme, J. Antony, S. Ehrlich, H. Krieg, *J. Chem. Phys.*, 2010, **132**, DOI:  
10.1063/1.3382344.

9 42. S. Grimme, S. Ehrlich, L. Goerigk, *J. Comput. Chem.*, 2011, **32**, 1456–1465, DOI:  
10.1002/jcc.21759.

10 43. H. Kruse, S. Grimme, *J. Chem. Phys.*, 2012, **136**, DOI: [10.1063/1.3700154](https://doi.org/10.1063/1.3700154).

11 44. O. Borodin, W. Behl, T. R. Jow, *J. Phys. Chem. C*, 2013, **117**, 8661–8682, DOI:  
10.1021/jp400527c.

12 45. J. Wang, Y. Wang, *J. Phys. Chem. B*, 2024, **128**, 1943–1952, DOI:  
10.1021/acs.jpcb.3c08127.

View Article Online  
DOI: 10.1039/D5DT02781K

1 46. V. Barone, M. Cossi, *J. Phys. Chem. A*, 1998, **102**, 1995–2001, DOI:  
2 10.1021/jp9716997.

3 47. C. F. Riadigos, R. Iglesias, M. A. Rivas and T. P. Iglesias, *J. Chem. Thermodyn.*,  
4 2011, **43**, 275–283, DOI: 10.1016/j.jct.2010.09.008.

5 48. T. Mandai, K. Yoshida, S. Tsuzuki, R. Nozawa, H. Masu, K. Ueno, K. Dokko and M.  
6 Watanabe, *J. Phys. Chem. B*, 2015, **119**, 1523–1534, DOI: 10.1021/jp508100s.

7 49. T. Mandai, K. Yoshida, K. Ueno, K. Dokko and M. Watanabe, *Phys. Chem. Chem.  
8 Phys.*, 2014, **16**, 8761–8772, DOI: 10.1039/c4cp00461b.

9 50. P. Johansson, J. Grondin, J.-C. Lassègues, *J. Phys. Chem. A*, 2010, **114**, 10700–10705,  
10 DOI: 10.1021/jp105437d.

11 51. L. Xue, C. W. Padgett, D. D. Desmartheau, W. T. Pennington, *Solid State Sci.*, 2002, **4**,  
12 1535–1545, DOI: 10.1016/S1293-2558(02)00050-X.

**Data availability statement**

[View Article Online](#)  
DOI: 10.1039/D5DT02781K

The data supporting this article have been included as part of the Supplementary Information.